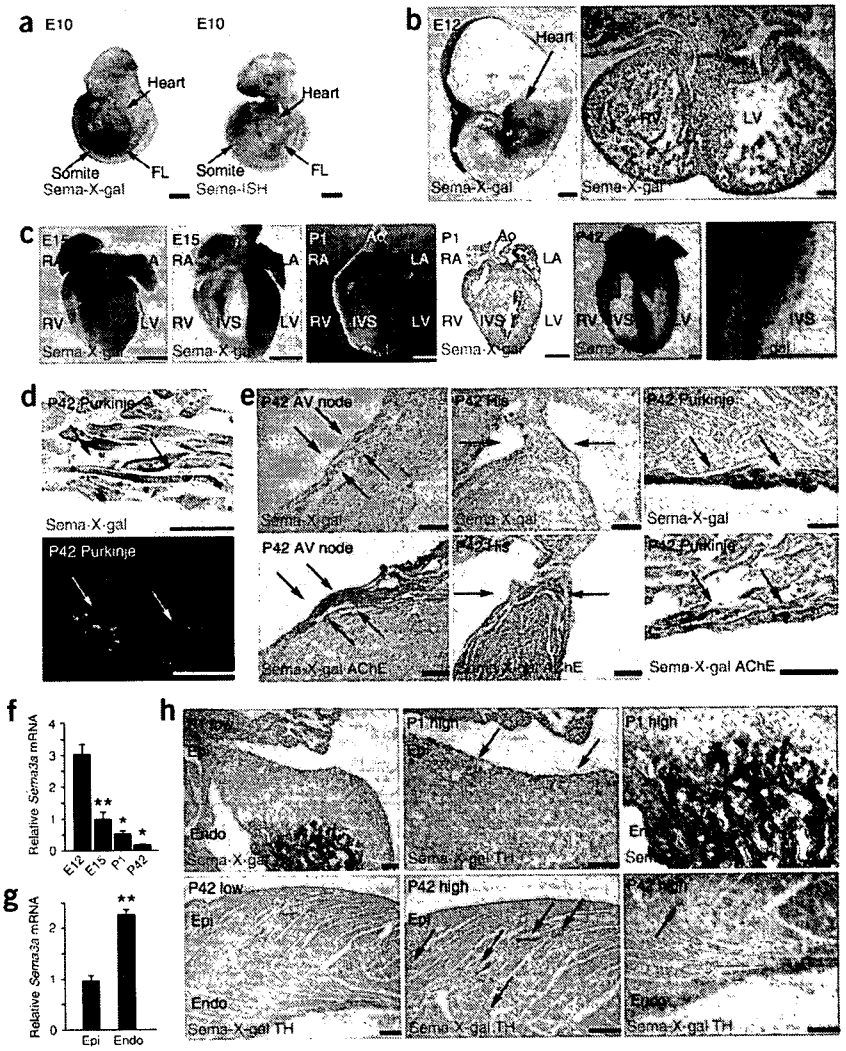

Figure 2 Inverse pattern of *Sema3a* expression and sympathetic innervation in developing hearts. (**a**) X-gal staining (green) of *Sema3a*$^{lacZ/+}$ at E10 (left). *In situ* hybridization (ISH) for *Sema3a* (right). (**b**) X-gal staining of *Sema3a*$^{lacZ/+}$ at E12 demonstrated strong *Sema3a* expression in the heart. (**c**) *lacZ* expression was observed in the subendocardium in *Sema3a*$^{lacZ/+}$ hearts at E15. The signal-positive areas were gradually reduced by P1 and P42, and a higher magnification view of the network of Purkinje fibers in P42 *Sema3a*$^{lacZ/+}$ hearts is shown in the far right micrograph. (**d**) X-gal staining (top) and triple immunofluorescence staining for α-actinin, Cx40 and TOTO3 (bottom) in the subendocardium in P42 *Sema3a*$^{lacZ/+}$ hearts. Arrows indicate Purkinje fibers demarcated with Cx40. (**e**) X-gal staining (top), and double staining with AChE (brown) and X-gal (blue) (bottom) for the conduction system (arrows) in P42 *Sema3a*$^{lacZ/+}$ hearts. Note that AChE-positive AV node and His bundle did not express *lacZ*, but AChE-positive Purkinje fibers were colabeled with X-gal staining. (**f**) *Sema3a* mRNA expression in wild-type developing hearts determined by quantitative RT-PCR ($n = 5$). (**g**) *Sema3a* expression in the subendocardium and subepicardium in wild-type mice ($n = 5$). (**h**) Double staining with tyrosine hydroxylase (TH, brown) and X-gal (blue) in P1 and P42 *Sema3a*$^{lacZ/+}$ hearts. 'Low' and 'high' indicate low and high magnification, respectively. Note that sympathetic nerves were restricted to the subepicardium at P1, but extended into the myocardium at P42, coincident with downregulation of Sema3a. Representative data are shown in **a**–**e** and **h**. $^{*}P < 0.001$ and $^{**}P < 0.01$ (in **f**, compared to data at E12). FL, forelimb; RA, right atrium; LA, left atrium; RV, right ventricle; LV, left ventricle; IVS, interventricular septum; Ao, aorta. Scale bars: 50 μm in **d**; 100 μm in the right panel of **b**; 100 μm in **e**,**h**; 1 mm in all others.

in the subendocardium in *Sema3a*$^{-/-}$ mice, resulting in a marked reduction of the subepicardial-to-subendocardial ratio of sympathetic innervation (7.7-fold in wild-type and 0.8-fold in *Sema3a*$^{-/-}$ animals **Fig. 3d–f**).

Next, we performed double staining with X-gal and tyrosine hydroxylase in *Sema3a*$^{lacZ/+}$ (*Sema3a* heterozygous null) and *Sema3a*$^{lacZ/lacZ}$ (*Sema3a* homozygous null) hearts. *Sema3a*$^{lacZ/+}$ hearts showed a restricted sympathetic innervation within the working myocardium, and the axons never extended into the *Sema3a*-expressing Purkinje fibers. In *Sema3a*$^{lacZ/lacZ}$ hearts, we observed many aberrant projections at the subendocardium where *lacZ* was expressed, and sympathetic nerves grew freely over *lacZ*-expressing areas (**Fig. 3g**). These results indicated that Sema3a is critical for the patterning of cardiac sympathetic innervation.

Sema3a$^{-/-}$ mice exhibit sinus bradycardia

We next examined the central conduction system in *Sema3a*$^{-/-}$ hearts. The sinoatrial nodes, atrioventricular nodes and His bundles, demarcated with AChE activity staining, were intact in appearance in *Sema3a*$^{-/-}$ hearts. The sympathetic nerve density in the conduction system was also not different between wild-type and *Sema3a*$^{-/-}$ hearts (**Fig. 4a** and **Supplementary Fig. 2** online). To determine whether sympathetic neurons that project nerve fibers to the heart were disrupted, we examined the stellate ganglia. TH^{+} neurons accumulated to form sympathetic ganglia at positions bilateral to the vertebrae in wild type mice. In contrast, the sympathetic neurons did not accumulate in *Sema3a*$^{-/-}$ mice but instead were distributed widely in a dislocated pattern (**Fig. 4b**). The stellate ganglia malformation was sustained at P42 in *Sema3a*$^{-/-}$ mice (data not shown).

To identify the effects of abnormal sympathetic neural distribution in the absence of Sema3a expression, we performed telemetric electrocardiography (ECG) in awake and free-moving wild-type and *Sema3a*$^{-/-}$ mice ($n = 5$ in both groups), of age 6 to 8 weeks. *Sema3a*$^{-/-}$ mice showed sinus bradycardia and abrupt sinus slowing, with a heart rate of 531 ± 27 beats per min compared with 604 ± 36 beats per min in wild-type mice (**Fig. 4c** and **Supplementary Table 1** online). To determine whether the bradycardia arose from intrinsic or extrinsic defects in the sinus node, we measured heart rate responses following pharmacological intervention. Blocking the sympathetic system with propranolol reduced the heart rate to a larger extent in the wild-type mice than in *Sema3a*$^{-/-}$ mice, suggesting that basal sympathetic activity was downregulated in *Sema3a*$^{-/-}$ hearts. In contrast, blocking parasympathetic activity had no substantial effect in either group of mice, consistent with previous reports showing that mice have weak

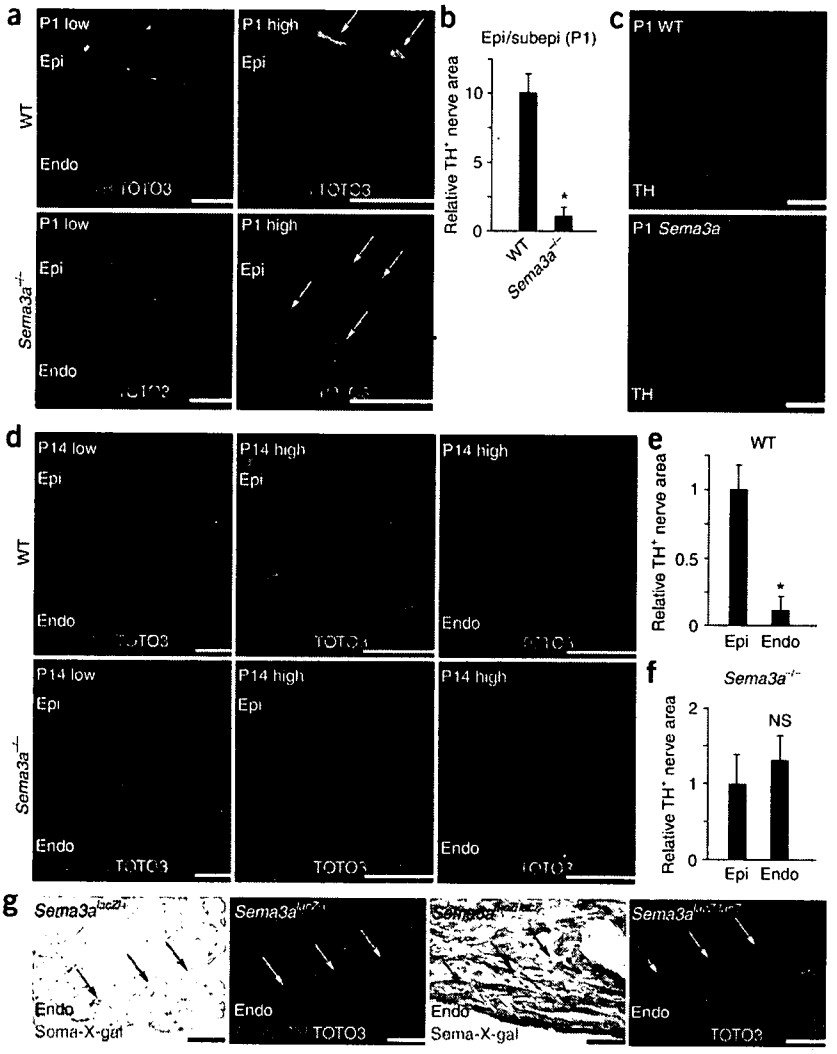

Figure 3 Cardiac sympathetic innervation patterning is disrupted in *Sema3a*-deficient mice. (**a**) Triple immunostaining for α-actinin, tyrosine hydroxylase (TH) and TOTO3 in P1 wild-type and *Sema3a*$^{-/-}$ hearts (low- and high-power fields). Arrows indicate sympathetic nerves. (**b**) Quantitative analysis of TH$^+$ nerve area in the epicardium and subepicardium in wild-type (WT) and *Sema3a*$^{-/-}$ hearts at P1 ($n = 5$). (**c**) Whole-mount immunofluorescence staining for TH in wild-type and *Sema3a*$^{-/-}$ hearts at P1. (**d**) Triple immunostaining for α-actinin, TH and TOTO3 in P14 wild-type and *Sema3a*$^{-/-}$ hearts (low- and high-power fields). An epicardial-to-endocardial gradient of sympathetic innervation was observed in wild-type hearts, but not in *Sema3a*$^{-/-}$ hearts, at P14. (**e,f**) Quantitative analysis of TH$^+$ nerve area in the subepicardium and subendocardium in wild-type and *Sema3a*$^{-/-}$ mice at P14 ($n = 5$). (**g**) Comparisons between X-gal and TH staining in P14 *Sema3a*$^{lacZ/+}$ and *Sema3a*$^{lacZ/lacZ}$ hearts are shown. Many aberrant nerves were observed in the *lacZ*-expressing area only in *Sema3a*$^{lacZ/lacZ}$ hearts (*Sema3a* homozygous null). Arrows indicate the *Sema3a*-expressing area visualized by *lacZ* expression. Representative data are shown in **a,c,d** and **g**. $^*P < 0.01$; NS, not significant. Scale bars, 100 μm.

parasympathetic activity[21,22]. The intrinsic heart rate, determined by blocking both autonomic activities, was not different between the two groups, suggesting that *Sema3a*$^{-/-}$ hearts retained intrinsic sinus node function (**Fig. 4d**). To further elucidate the autonomic activities, we performed a heart rate variability (HRV) analysis. Spectral analysis revealed a significant reduction in normalized low filtration (NLF) and in the low-to-high filtration (LF-to-HF) ratio (markers of sympathetic activity) and an increase in normalized high filtration (NHF) in *Sema3a*$^{-/-}$ mice (**Fig. 4e–g**). Thus, the intrinsic sinus node function (a cell-autonomous effect) was preserved, but sympathetic neural activity (a cell-non-autonomous effect) was significantly downregulated in *Sema3a*$^{-/-}$ hearts, presumably owing to malformation of sympathetic ganglia. These results indicated that *Sema3a*$^{-/-}$ mice develop sinus bradycardia as a result of sympathetic neural dysfunction. *Sema3a*$^{-/-}$ mice also showed spontaneous premature ventricular contractions (PVCs) (*Sema3a*$^{-/-}$: 2 of 10 mice; wild-type: 0 of 10 mice) (**Fig. 4h**). However, sustained ventricular tachycardia was not observed in either group before or after epinephrine injection.

Cardiac-specific *Sema3a* overexpression reduces innervation

It is possible that the abnormal patterning of cardiac sympathetic nerves in *Sema3a*-deficient hearts was a secondary effect of the malformation of sympathetic ganglia. To address this, we generated cardiac-specific transgenic mice expressing *Sema3a* (*SemaTG*) under the control of an α-myosin heavy chain promoter[23]. Northern blot analysis revealed that *Sema3a* was expressed exclusively in the heart. The expression of other factors known to be involved in sympathetic innervation, such as NGF and vascular endothelial growth factor-A, was unaffected in *SemaTG* mice (**Fig. 5a**). The growth cone collapse assay revealed that media conditioned with *SemaTG* cardiomyocytes had strong chemorepellent effects on sympathetic nerves, indicating that bioactive Sema3a was secreted from *SemaTG* cardiomyocytes (refs. 24,25 and **Fig. 5b**). *In situ* hybridization for *Sema3a* demonstrated *Sema3a* expression only at the subendocardium, not at the mid- or subepicardium, in wild-type hearts, similar to the results for *Sema3a*$^{lacZ/+}$ hearts. In contrast, *Sema3a* was expressed throughout the ventricles in *SemaTG* mice and showed higher expression at the subendocardium and midcardium than at the subepicardium in the ventricles. There was no *Sema3a* expression in the atrioventricular nodes or His bundles in either genotype (**Fig. 5c** and **Supplementary Fig. 3** online). Echocardiography and histology did not identify any contractile dysfunction or structural defects in *SemaTG* hearts.

To determine whether sympathetic innervation was altered in *SemaTG* mice, we immunostained mouse hearts with an antibody to tyrosine hydroxylase and measured the norepinephrine concentration in the ventricles (**Fig. 5d,e** and **Supplementary Fig. 3**). In *SemaTG* ventricles, sympathetic innervation was markedly reduced and the total cardiac norepinephrine concentration was reduced by 76%. Sympathetic innervation of the sinoatrial nodes, atrioventricular nodes and His bundles was not altered in *SemaTG* hearts (data not shown). We next analyzed the transmural difference of sympathetic innervation in *SemaTG* hearts. TH$^+$ nerve fibers and norepinephrine

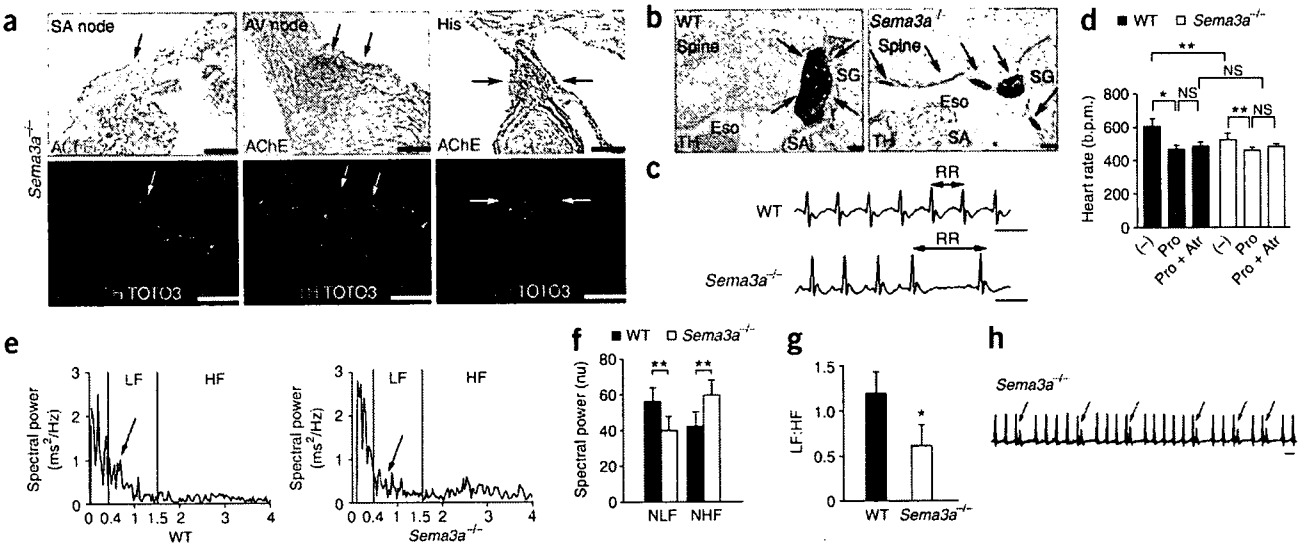

Figure 4 *Sema3a*-deficient mice display malformation of stellate ganglia and sinus bradycardia. (**a**) Top, AChE (brown) and hematoxylin (purple) staining. Bottom, immunostaining of sinoatrial node, atrioventricular node and His bundle (arrows) in P14 *Sema3a*$^{-/-}$ hearts with α-actinin, tyrosine hydroxylase (TH) and TOTO3. (**b**) Stellate ganglia (SG, arrows) in P1 animals were observed by TH immunostaining (brown). Note that a single SG was observed at a position lateral to the spine in wild-type mice, but that multiple SG were distributed widely in a dislocated pattern in *Sema3a*$^{-/-}$ mice Eso, esophagus; SA, subclavian artery. (**c**) ECG recordings from wild-type and *Sema3a*$^{-/-}$ mice. The lengthened RR interval indicates abrupt sinus slowing in *Sema3a*$^{-/-}$ mice. (**d**) Changes in heart rate following pharmacological modifications in wild-type and *Sema3a*$^{-/-}$ mice ($n = 5$). Note that propranolol reduced heart rate to a lesser extent in *Sema3a*$^{-/-}$ mice than in wild-type mice. (–), no addition; Pro, propranolol; Pro + Atr, propranolol + atropine. (**e**) Power spectra of heart-rate variability (HRV) in wild-type and *Sema3a*$^{-/-}$ mice. Note decrease of HRV across low filtration (LF) band in *Sema3a*$^{-/-}$ mice, reflecting lower sympathetic nerve activity (arrows). (**f**,**g**) The normalized low filtration (NLF) and the low-to-high filtration (LF:HF) ratio were decreased in *Sema3a*$^{-/-}$ mice ($n = 5$). (**h**) Spontaneous and frequent premature ventricular contractions (PVCs, arrows) were observed in *Sema3a*$^{-/-}$ mice. Representative data are shown in **a**–**c**, **e** and **h**. $^{*}P < 0.01$; $^{**}P < 0.05$; NS, not significant. Scale bars: 100 μm in **a**,**b**; 100 ms in **c**,**h**.

concentration were decreased proportionally at both the subepicardium and subendocardium in *SemaTG* ventricles (**Fig. 5f,g**). Therefore, sympathetic innervation density was inversely proportional to *Sema3a* expression in *SemaTG* hearts. The appearance of stellate ganglia was not different between wild-type and *SemaTG* mice (**Fig. 5h**). These results indicated that cardiomyocyte-derived Sema3a mediates repulsive and inhibitory effects on cardiac sympathetic neural growth.

SemaTG mice are susceptible to ventricular arrhythmias

The *SemaTG* mice died suddenly, without any symptoms, at 10 months of age (4 of 22 *SemaTG* mice versus 0 of 22 wild-type mice) (**Fig. 6a**), and necropsy showed no abnormalities. Telemetry ECG revealed spontaneous PVCs in *SemaTG* mice but not in wild-type mice (3 of 10 *SemaTG* mice versus 0 of 10 wild-type mice), whereas there were no significant differences in other ECG parameters (**Fig. 6b** and **Supplementary Table 2** online). Epinephrine administration induced multiple nonsustained and sustained episodes of ventricular tachycardia in the *SemaTG* mice only (2 of 10 *SemaTG* mice versus 0 of 10 wild-type mice) (**Fig. 6c**). To further characterize susceptibility to arrhythmia, we subjected wild-type and *SemaTG* mice to programmed electrical stimulation. *SemaTG* mice had nonsustained ventricular tachycardia at baseline, the frequency and duration of which were significantly increased by a low dose of isoproterenol (**Fig. 6d,e**; 8 of 10 *SemaTG* mice). In contrast, no wild-type mice ($n = 10$) developed sustained ventricular tachycardia. There were no electrophysiological differences between the two groups (**Supplementary Table 2**).

It is possible that the hypoinnervated *SemaTG* hearts showed ventricular arrhythmias as a result of catecholamine supersensitivity. To test this possibility, we measured cyclic AMP (cAMP) levels in wild-type and *SemaTG* ventricles before and after isoproterenol injection. Although basal cAMP levels were not different, the increase in cAMP after isoproterenol administration was greater in *SemaTG* mice than wild-type mice, indicating an augmented adrenergic response in *SemaTG* hearts (**Fig. 6f**). To investigate this mechanistically, we measured the density of the β_1-adrenergic receptor (β_1AR) in the ventricles. The β_1AR density was 1.5-fold greater in *SemaTG* ventricles (**Fig. 6g**).

We next investigated the transmembrane action potential of left ventricular myocytes, using glass microelectrodes. Action potential duration (APD) assessed at 50% and 90% repolarization (APD_{50} and APD_{90}) were shorter in the subepicardium than in the subendocardium in the wild-type mice. APD was significantly prolonged in hypoinnervated *SemaTG* subepicardium and subendocardium, and was inversely proportional to sympathetic innervation density. The action potential amplitude, resting membrane potential and maximum positive deflection of phase 0 upstroke were not altered, indicating that repolarization currents were disrupted in *SemaTG* hearts (**Fig. 6h**). These results suggested that the higher susceptibility of *SemaTG* mice to ventricular arrhythmia was due to catecholamine supersensitivity and APD prolongation, both of which might augment triggered activity in cardiomyocytes.

DISCUSSION

This work shows that a gradient of the neural chemorepellent Sema3a is essential for proper cardiac sympathetic innervation patterning, and that inappropriate Sema3a expression triggers various kinds of arrhythmias as a result of the disruption of this patterning. To our knowledge, this is the first identification of a critical regulatory

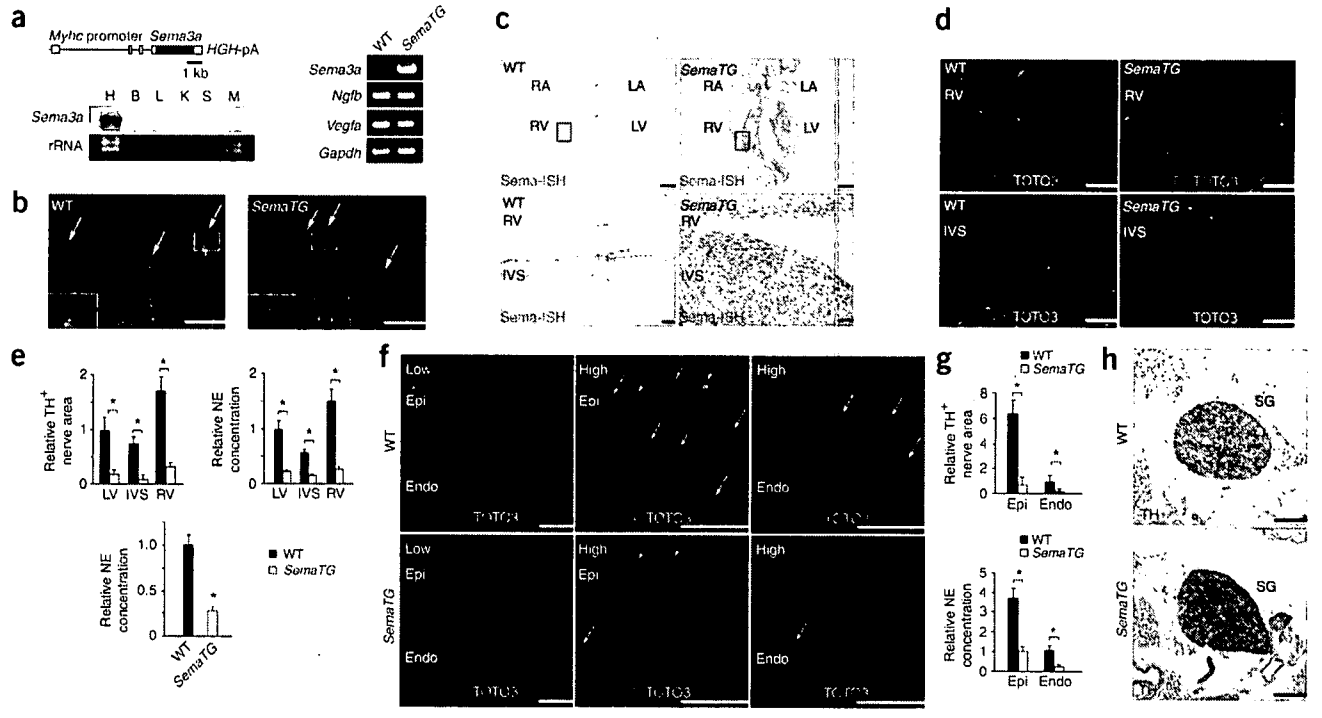

Figure 5 Cardiac sympathetic innervation patterning was disturbed in *SemaTG* hearts. (**a**) Schematic representation of the transgene containing the α-myosin heavy chain (*Myhc*) promoter, mouse *Sema3a* cDNA and human growth hormone (*HGH*) polyadenylation signal (pA). Northern blot analysis for *Sema3a* in *SemaTG* mice and RT-PCR analysis of *Sema3a*, *Ngfb*, *Vegfa* and *Gapdh* in wild-type and *SemaTG* hearts are shown. H, heart; B, brain; L, liver; K, kidney; S, spleen; M, muscle. (**b**) Growth cone collapse assay, visualized with GAP43 immunostaining. Arrows indicate growth cones. Insets show high-power views of the boxed areas. (**c**) *In situ* hybridization (ISH) for *Sema3a* in wild-type and *SemaTG* hearts. High-power views of the boxed areas are shown in the lower micrographs. (**d**) Triple immunofluorescence staining for α-actinin, tyrosine hydroxylase (TH) and TOTO3 in wild-type and *SemaTG* hearts. (**e**) TH^+ nerve areas were decreased in *SemaTG* hearts ($n = 5$). Cardiac norepinephrine (NE) concentrations were also reduced in *SemaTG* ventricles compared with wild-type ventricles ($n = 8$). (**f**) Triple immunofluorescence staining for α-actinin, TH and TOTO3 in wild-type and *SemaTG* hearts. The number of TH^+ nerves was decreased in both the subepicardium (Epi) and the subendocardium (Endo) in *SemaTG* ventricles. Arrows indicate TH^+ nerves. (**g**) Quantitative analysis of TH^+ nerve area and norepinephrine concentrations in the subepicardium and the subendocardium ($n = 5$). (**h**) Stellate ganglia (SG) were not abnormal in *SemaTG* mice. Representative data are shown in **b–d**,**f** and **h**. LV, left ventricle; IVS, interventricular septum; RV, right ventricle; RA, right atrium; LA, left atrium. All mice were analyzed at 6 weeks of age. * $P < 0.01$. Scale bars: 50 μm in **b**,**d**; 100 μm in lower panels of **c**; 100 μm in **f**,**h**; 1 mm in top panels of **c**.

factor for cardiac sympathetic patterning. The expression pattern of Sema3a in the heart is inversely related to sympathetic innervation. Sympathetic nerves express both the NGF receptor TrkA and the Sema3a receptor neuropilin-1 (refs. 14,24). During development, NGF and Sema3a are expressed within the spinal cord and influence pathway guidance of sensory axons. Sema3a is specifically expressed in the ventral half of the spinal cord and induces NGF-responsive sensory axons to terminate at the dorsal part of the spinal cord[13,26]. Thus, the growth cone behavior of sensory axons is modulated by coincident signaling between NGF and Sema3a (ref. 27). As cardiomyocyte-derived NGF acts as a chemoattractant and Sema3a is a potent chemorepellent for sympathetic nerves, it might be the balance between NGF and Sema3a synthesized in the heart that determines cardiac sympathetic innervation patterning. The phenotype of *Sema3a*$^{-/-}$ hearts strongly suggests that no other semaphorin ligands can compensate for loss of *Sema3* function in the control of cardiac sympathetic neural patterning.

Sema3a promotes the aggregation of neurons into sympathetic ganglia during early embryogenesis. This was demonstrated previously with displacement of sympathetic neurons and abnormal morphogenesis of the sympathetic trunk in *Sema3a*$^{-/-}$ mice observed at E12.5 (ref. 14). However, little is known about the role of Sema3a after birth. We found a sustained deficiency in sympathetic neural patterning in *Sema3a*$^{-/-}$ hearts and dislocation of stellate ganglia at P1 and P42. Sympathetic nerve density was inversely proportional to Sema3a expression in *SemaTG* hearts, in which Sema3a is expressed mainly after birth. These results indicate that endogenous Sema3a is crucial for the cardiac sympathetic patterning, not only during embryonic development but also after birth.

Sympathetic nerves modulate the function of ion channels and trigger various types of arrhythmias in diseased hearts[28,29]. However, the relationship between sympathetic innervation and arrhythmogenicity in structurally normal hearts remains unclear. *Sema3a*$^{-/-}$ mice exhibited sinus bradycardia, abrupt sinus slowing and stellate ganglia defects. Pharmacological and HRV analysis confirmed a reduced sympathetic nerve activity in *Sema3a*$^{-/-}$ hearts. Consistent with our results, right stellectomy induces sinus bradycardia and sudden, asystolic death in dogs[30,31]. *SemaTG* hearts were also highly susceptible to ventricular arrhythmias, although without contractile dysfunction or structural defects. Given that catecholamine augments systolic function, it is surprising that *SemaTG* hearts showed normal cardiac function. However, consistent with our results, patients who underwent heart transplantation and had denervated hearts did not show heart failure, whereas about 10% of the patients developed sudden

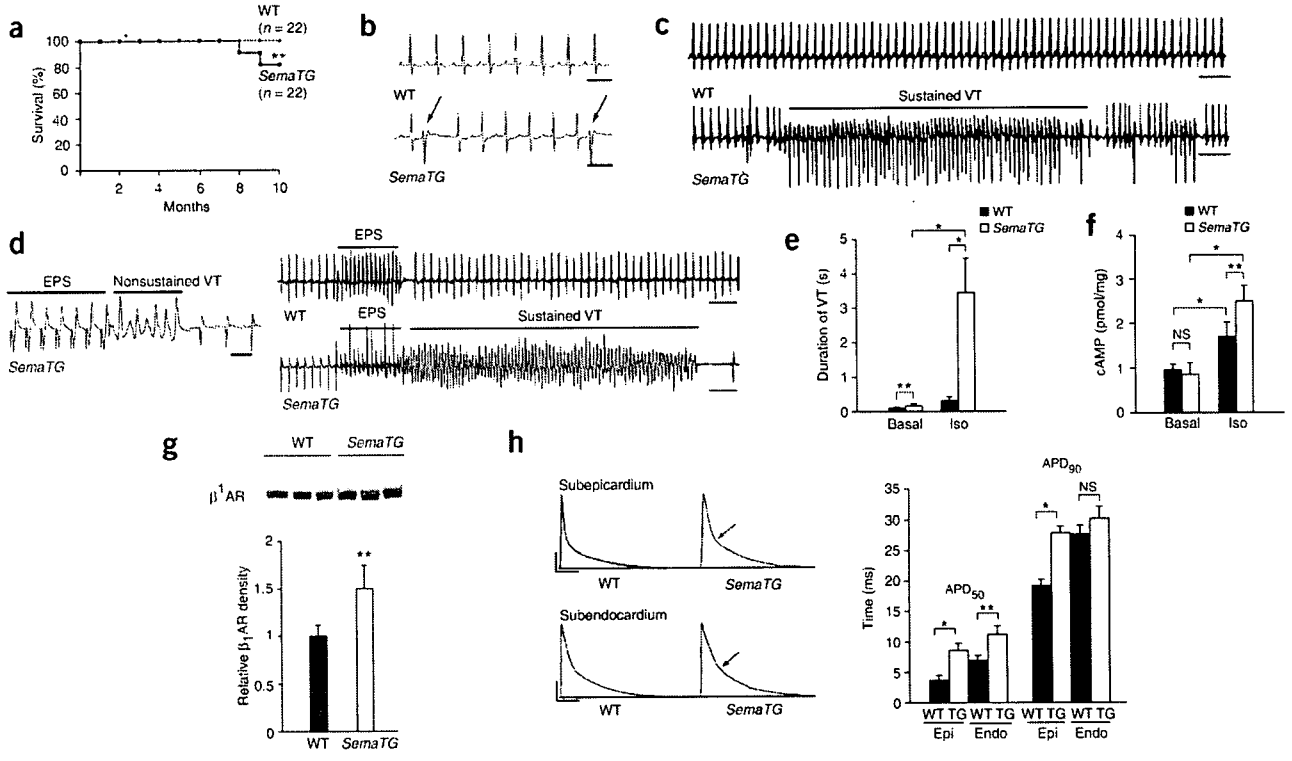

Figure 6 *SemaTG* mice are highly susceptible to induction of ventricular arrhythmia. (**a**) Survival curves of wild-type and *SemaTG* mice. (**b**) Spontaneous PVCs (arrows) were frequently observed in *SemaTG* mice. (**c**) Epinephrine administration revealed sustained ventricular tachycardia (VT) only in *SemaTG* mice. (**d**) Surface ECG during programmed electrical stimulation (EPS) showing nonsustained VT at baseline, and sustained VT after administration of isoproterenol in *SemaTG* mice. The heart was paced epicardially at an S1-S1 interval of 80 ms, followed by a premature beat of 50 ms at an S1-S2 interval. (**e**) Average duration of VT episodes before and after isoproterenol (Iso) ($n = 10$). (**f**) Intracellular concentration of cAMP at basal levels and after isoproterenol administration in wild-type and *SemaTG* hearts ($n = 5$). (**g**) Immunoblotting showed increased β_1AR levels in membrane fractions from *SemaTG* hearts. The relative β_1AR density is shown ($n = 5$). (**h**) Representative action potential tracing from wild-type and *SemaTG* subepicardium (Epi) and subendocardium (Endo). *SemaTG* subepicardium and subendocardium showed prolonged action potentials (arrows). Mean APD measured at 50% and 90% repolarization in wild-type and *SemaTG* (TG) hearts is shown (APD_{50} and APD_{90}; $n = 10$). Representative data are shown in **b–d,g** and **h**. Mice were analyzed at 6 to 8 weeks of age (**b–h**). $^*P < 0.01$; $^{**}P < 0.05$; NS, not significant. Scale bars: 20 ms and 20 mV in **h**; 100 ms in **b** and left panel of **d**; 500 ms in **c** and right panel of **d**.

cardiac death, presumably due to arrhythmias[32]. We also observed similar basal cAMP levels and upregulation of β_1AR in *SemaTG* hearts compared with wild-type hearts. These data therefore strongly support the idea that sympathetic nerves contribute to the fine control of cardiac performance on demand, but not to basal cardiac function. The findings that both the induction of ventricular tachycardia and the production of cAMP were enhanced by isoproterenol, and that *SemaTG* hearts were severely hypoinnervated, implicate adrenergic denervation supersensitivity as a cause of arrhythmogenicity in *SemaTG* mice. It is possible that Sema3a acts directly on cardiomyocytes, but we consider this unlikely, as its receptor neuropilin-1 is expressed in cardiomyocytes only at low levels[33,34]. Action potential duration was inversely proportional to sympathetic innervation density in wild-type and *SemaTG* ventricles, suggesting that sympathetic innervation might regulate repolarization currents. Given that the electrical properties of ventricular myocytes are heterogeneous and that the cardiac repolarization gradient is highly organized through a transmural structure in ventricles[35–37], it would be intriguing to investigate the relationship between sympathetic innervation patterning and the ventricular repolarization gradient.

In conclusion, our results indicate that normal sympathetic innervation patterning mediated by Sema3a is important for the maintenance of arrhythmia-free hearts. Knowledge of the mechanisms regulating sympathetic patterning in hearts may represent a new step toward potential therapies for lethal arrhythmia.

METHODS

Animals. *Sema3a*$^{-/-}$ mice and *Sema3a* knocked-in *lacZ* mice were generated as described previously[16].

Generation of transgenic mice expressing *Sema3a* in the heart. The *Sema3a* cDNA was subcloned into an expression vector containing the α-myosin heavy chain promoter[23]. Pronuclear microinjection and other procedures were performed according to standard protocols of the Keio University Animal Care Center. The transgene was identified by PCR analysis (forward primer, 5′-GTGGTCCACATTCTTCAGGA-3′; reverse primer, 5′-GAGGCAGTCAG TAGTTTGGG-3′). All mice used in this study (*Sema3a*$^{-/-}$, *Sema3a*$^{lacZ/lacZ}$ and *SemaTG*) were backcrossed ten times into the C57BL/6 background. The Keio University Ethics Committee for Animal Experiments approved all experiments in this study.

Northern blot and quantitative RT-PCR. RNA was isolated from several tissues and from left ventricular subepicardial and subendocardial sections. For northern blot analysis, 20 μg of total RNA was used. The *Sema3a* cDNA was obtained from a C57BL/6 adult brain cDNA library as described previously[11]. Quantitative RT-PCR was performed with TaqMan probes (Applied Biosystems): *Sema3a* (Mm00436469_m1) and *Vegfa* (Mm00437304_m1). The

primers and probes for *Ngfb* were as described previously[11]. The mRNA levels were normalized by comparison to *Gapdh* mRNA.

Western blot analysis. Myocardial membrane fractions were prepared by homogenization of hearts in ice-cold buffer as described[38]. Immunodetection was performed on membrane extracts with an antibody to β_1AR (Affinity BioReagents) as previously described[38]. After transfer to nitrocellulose membranes, the 64-kDa β_1AR protein was visualized by chemiluminescence detection (ECL, Amersham).

Detection of growth cone collapse. Stellate ganglia explants were removed from E14 embryos and cultured in medium containing 10% FBS and NGF (Upstate)[39]. After 24 h incubation, the explants were cultured with cardiomyocyte-conditioned media. For detection of growth cone collapse, the cultures were immunostained with an antibody to GAP43 (Chemicon)[25]. Sema3a-Fc (R&D systems) was used as a positive control.

***In situ* hybridization.** *In situ* hybridization with digoxigenin-labeled mouse *Sema3a* antisense cRNA was performed on whole embryos and paraffin-embedded sections[14]. The bound probes were visualized with alkaline phosphatase–conjugated Fab fragment of antibody to digoxigenin (Boehringer Mannheim).

Norepinephrine measurement. Norepinephrine concentration was determined by high-performance liquid chromatography (HPLC) as described previously[11].

Immunohistochemistry of hearts. Hearts were perfused from the apex with 0.4% paraformaldehyde in phosphate-buffered saline, fixed overnight, and then embedded in optimal cutting temperature (OCT) compound and frozen in liquid nitrogen. Hearts were cut longitudinally in 5-μm sections near the central conduction system to show the four chambers. Cryostat sections were stained with antibodies to α-actinin (Sigma Aldrich), connexin40 (Chemicon) and tyrosine hydroxylase (Chemicon) to detect cardiomyocytes, Purkinje fibers and sympathetic nerve fibers, respectively. The sections were incubated with secondary antibodies conjugated with Alexa 488 or 594 (Molecular Probes) and the nuclei were stained with TOTO3 (Molecular Probes). All confocal microscopy was carried out on an LSM 510 META microscope (Carl Zeiss). In some experiments, paraffin-embedded sections were stained with an antibody to tyrosine hydroxylase. Following hybridization with the secondary antibody, sections were incubated with diaminobenzidine. Nerve density was determined as described previously[11]. Briefly, we defined an epicardial portion as an epicardial half of the ventricle and an endocardial portion as an endocardial half of the ventricle for each slide. Within each portion, the six fields that contained the most nerve fiber structures were analyzed. The nerve density was the ratio between the total area of nerves and the total myocardial area, each measured by Image J software. The data for each mouse were calculated from 30 to 40 serial sections. To determine the nerve density in the conduction system, the acetyl cholinesterase–positive or connexin40-positive demarcated areas were analyzed as above. For whole-mount immunostaining, hearts were fixed with 4% paraformaldehyde and stained with an antibody to tyrosine hydroxylase.

Histological analysis. Acetyl cholinesterase staining was performed to localize the central conduction system. For serial sections of the atrioventricular node and the His bundle, anatomical landmarks were used to help guide the decision to begin collection of the sections[18,19].

Electrocardiographic recordings. Telemetric ECG recordings were obtained from conscious adult mice using a wireless implantable transmitter manufactured by Data Sciences International. Mice were anesthetized with ketamine (30 mg/kg) and xylazine (6 mg/kg) and the transmitter was placed in the abdominal cavity. The limb leads were placed in the right arm and the left leg. After implantation of the transmitter, mice were allowed to recover for at least 72 h before data collection. The telemetry data was collected continuously for 2 d and analyzed using HEM 3.4 software (Notocord Systems). Propranolol (4 mg/kg) and atropine (1 mg/kg) were injected intraperitoneally, and changes were examined during 30 min before and after injection[21]. For catecholamine stimulation, epinephrine (2 mg/kg) was injected intraperitoneally[40].

Heart-rate variability (HRV) analysis. HRV analysis was conducted following standard guidelines as described previously[41,42]. Spectral analysis using a fast Fourier transform algorithm on sequences of 512 points was performed using the HEM 3.4 software. The area under the curve was calculated for the very-low-frequency (<0.4 Hz), low-frequency (LF: 0.4–1.5 Hz) and high-frequency (HF: 1.5–4.0 Hz) bands. Spectral variability at each bandwidth was normalized (NLF, NHF) to the total spectral area[41,42].

Electrophysiology. Mice were intubated and anesthetized with 0.5% isofluorane gas, and a surface ECG was recorded during the experiment. After midline sternotomy, a bipolar stimulating electrode was positioned on the left ventricular surface. Standard pacing protocols for electrical stimulation in mice were used[43,44]. Burst pacing and 15 rapid ventricular pacing at cycle lengths of 100 ms and 80 ms with extrastimulation were performed to determine the ventricular effective refractory period (VERP) and to induce ventricular arrhythmias (with single and double extrastimuli). If arrhythmias, such as nonsustained ventricular tachycardia (3–10 beats) or sustained ventricular tachycardia (>10 beats), were induced, the protocol was repeated to determine reproducibility. After baseline measurements were completed, isoproterenol (100 μg) was administered intraperitoneally and the protocols were repeated[43,44].

Statistical analysis. Values are presented as means ± s.e.m. Differences between groups were examined for statistical significance using Student's *t*-test or ANOVA. *P* values of < 0.05 were regarded as significant.

Other methods. Other methods are listed in the **Supplementary Methods** online.

GenBank accession number. Mouse *Sema3a*, NM_009152.

Note: Supplementary information is available on the Nature Medicine website.

ACKNOWLEDGMENTS

We are grateful to J. Robbins (Cincinnati Children's Hospital) for the expression vector containing the α-myosin heavy chain promoter. We also thank Y. Tanimoto, Y. Miyake, H. Kawaguchi, E. Kobayashi and M. Nakamura for technical assistance. We are also grateful to the members of the Fukuda laboratory for their comments on the manuscript. This study was supported in part by research grants from the Ministry of Education, Culture, Sports, Science and Technology, Japan, and the Program for Promotion of Fundamental Studies in Health Sciences of the National Institute of Biomedical Innovation.

AUTHOR CONTRIBUTIONS

M.I. designed the study, conducted all experiments, and wrote the manuscript. H.K. and K.K. conducted histochemical characterization. F.H. participated in subcloning. Y.I. conducted the growth cone collapse assay. M.T. provided *Sema3a*$^{-/-}$ mice and *Sema3a*$^{lacZ/lacZ}$ mice. S.M., J.-K.L and I.K participated in and provided advice on the electrophysiology. K.M. and Y.T. participated in histochemical characterization. K.S. conducted the pronuclear microinjection. S.M. and M.S. participated in northern blotting and western blotting. S.O. provided advice on the experimental design. K.F. supported financially and supervised the whole project.

COMPETING INTERESTS STATEMENT

The authors declare no competing financial interests.

Published online at http://www.nature.com/naturemedicine
Reprints and permissions information is available online at http://npg.nature.com/reprintsandpermissions

1. Crick, S.J. *et al.* Innervation of the human cardiac conduction system. A quantitative immunohistochemical and histochemical study. *Circulation* **89**, 1697–1708 (1994).
2. Randall, W.C., Szentivanyi, M., Pace, J.B., Wechsler, J.S. & Kaye, M.P. Patterns of sympathetic nerve projections onto the canine heart. *Circ. Res.* **22**, 315–323 (1968).
3. Ito, M. & Zipes, D.P. Efferent sympathetic and vagal innervation of the canine right ventricle. *Circulation* **90**, 1459–1468 (1994).
4. Crick, S.J., Sheppard, M.N., Ho, S.Y. & Anderson, R.H. Localisation and quantitation of autonomic innervation in the porcine heart I: conduction system. *J. Anat.* **195**, 341–357 (1999).
5. Chow, L.T., Chow, S.S., Anderson, R.H. & Gosling, J.A. Innervation of the human cardiac conduction system at birth. *Br. Heart J.* **69**, 430–435 (1993).

6. Hansson, M., Kjorell, U. & Forsgren, S. Increased immunoexpression of atrial natriuretic peptide in the heart conduction system of the rat after cardiac sympathectomy. *J. Mol. Cell. Cardiol.* **30**, 2047–2057 (1998).
7. Cao, J.M. *et al.* Nerve sprouting and sudden cardiac death. *Circ. Res.* **86**, 816–821 (2000).
8. Cao, J.M. *et al.* Relationship between regional cardiac hyperinnervation and ventricular arrhythmia. *Circulation* **101**, 1960–1969 (2000).
9. Opthof, T. *et al.* Dispersion of refractoriness in canine ventricular myocardium. Effects of sympathetic stimulation. *Circ. Res.* **68**, 1204–1215 (1991).
10. Priori, S.G. & Corr, P.B. Mechanisms underlying early and delayed afterdepolarizations induced by catecholamines. *Am. J. Physiol.* **258**, H1796–H1805 (1990).
11. Ieda, M. *et al.* Endothelin-1 regulates cardiac sympathetic innervation in the rodent heart by controlling nerve growth factor expression. *J. Clin. Invest.* **113**, 876–884 (2004).
12. Kuruvilla, R. *et al.* A neurotrophin signaling cascade coordinates sympathetic neuron development through differential control of TrkA trafficking and retrograde signaling. *Cell* **118**, 243–255 (2004).
13. Puschel, A.W., Adams, R.H. & Betz, H. Murine semaphorin D/collapsin is a member of a diverse gene family and creates domains inhibitory for axonal extension. *Neuron* **14**, 941–948 (1995).
14. Kawasaki, T. *et al.* Requirement of neuropilin 1-mediated Sema3A signals in patterning of the sympathetic nervous system. *Development* **129**, 671–680 (2002).
15. Tanelian, D.L., Barry, M.A., Johnston, S.A., Le, T. & Smith, G.M. Semaphorin III can repulse and inhibit adult sensory afferents *in vivo*. *Nat. Med.* **3**, 1398–1401 (1997).
16. Taniguchi, M. *et al.* Disruption of semaphorin III/D gene causes severe abnormality in peripheral nerve projection. *Neuron* **19**, 519–530 (1997).
17. Behar, O., Golden, J.A., Mashimo, H., Schoen, F.J. & Fishman, M.C. Semaphorin III is needed for normal patterning and growth of nerves, bones and heart. *Nature* **383**, 525–528 (1996).
18. Pashmforoush, M. *et al.* Nkx2–5 pathways and congenital heart disease; loss of ventricular myocyte lineage specification leads to progressive cardiomyopathy and complete heart block. *Cell* **117**, 373–386 (2004).
19. Tago, H., Kimura, H. & Maeda, T. Visualization of detailed acetylcholinesterase fiber and neuron staining in rat brain by a sensitive histochemical procedure. *J. Histochem. Cytochem.* **34**, 1431–1438 (1986).
20. Kupershmidt, S. *et al.* Replacement by homologous recombination of the minK gene with lacZ reveals restriction of minK expression to the mouse cardiac conduction system. *Circ. Res.* **84**, 146–152 (1999).
21. Shusterman, V. *et al.* Strain-specific patterns of autonomic nervous system activity and heart failure susceptibility in mice. *Am. J. Physiol. Heart Circ. Physiol.* **282**, H2076–H2083 (2002).
22. Saba, S., London, B. & Ganz, L. Autonomic blockade unmasks maturational differences in rate-dependent atrioventricular nodal conduction and facilitation in the mouse. *J. Cardiovasc. Electrophysiol.* **14**, 191–195 (2003).
23. Gulick, J., Subramaniam, A., Neumann, J. & Robbins, J. Isolation and characterization of the mouse cardiac myosin heavy chain genes. *J. Biol. Chem.* **266**, 9180–9185 (1991).
24. Kitsukawa, T. *et al.* Neuropilin-semaphorin III/D-mediated chemorepulsive signals play a crucial role in peripheral nerve projection in mice. *Neuron* **19**, 995–1005 (1997).
25. Xu, X.M. *et al.* The transmembrane protein semaphorin 6A repels embryonic sympathetic axons. *J. Neurosci.* **20**, 2638–2648 (2000).
26. Wright, D.E., White, F.A., Gerfen, R.W., Silos-Santiago, I. & Snider, W.D. The guidance molecule semaphorin III is expressed in regions of spinal cord and periphery avoided by growing sensory axons. *J. Comp. Neurol.* **361**, 321–333 (1995).
27. Tang, X.Q., Tanelian, D.L. & Smith, G.M. Semaphorin3A inhibits nerve growth factor-induced sprouting of nociceptive afferents in adult rat spinal cord. *J. Neurosci.* **24**, 819–827 (2004).
28. Dae, M.W. *et al.* Heterogeneous sympathetic innervation in German shepherd dogs with inherited ventricular arrhythmia and sudden cardiac death. *Circulation* **96**, 1337–1342 (1997).
29. Qu, J. & Robinson, R.B. Cardiac ion channel expression and regulation: the role of innervation. *J. Mol. Cell. Cardiol.* **37**, 439–448 (2004).
30. Sosunov, E.A. *et al.* Long-term electrophysiological effects of regional cardiac sympathetic denervation of the neonatal dog. *Cardiovasc. Res.* **51**, 659–669 (2001).
31. Stramba-Badiale, M., Lazzarotti, M. & Schwartz, P.J. Development of cardiac innervation, ventricular fibrillation, and sudden infant death syndrome. *Am. J. Physiol.* **263**, H1514–H1522 (1992).
32. Chantranuwat, C. *et al.* Sudden, unexpected death in cardiac transplant recipients: an autopsy study. *J. Heart Lung Transplant.* **23**, 683–689 (2004).
33. Gitler, A.D., Lu, M.M. & Epstein, J.A. PlexinD1 and semaphorin signaling are required in endothelial cells for cardiovascular development. *Dev. Cell* **7**, 107–116 (2004).
34. Gu, C. *et al.* Neuropilin-1 conveys semaphorin and VEGF signaling during neural and cardiovascular development. *Dev. Cell* **5**, 45–57 (2003).
35. Kuo, H.C. *et al.* A defect in the Kv channel-interacting protein 2 (KChIP2) gene leads to a complete loss of I(to) and confers susceptibility to ventricular tachycardia. *Cell* **107**, 801–813 (2001).
36. Brunet, S. *et al.* Heterogeneous expression of repolarizing, voltage-gated K+ currents in adult mouse ventricles. *J. Physiol. (Lond.)* **559**, 103–120 (2004).
37. Costantini, D.L. *et al.* The homeodomain transcription factor Irx5 establishes the mouse cardiac ventricular repolarization gradient. *Cell* **123**, 347–358 (2005).
38. Takahashi, T. *et al.* Increased cardiac adenylyl cyclase expression is associated with increased survival after myocardial infarction. *Circulation* **114**, 388–396 (2006).
39. Patel, T.D., Jackman, A., Rice, F.L., Kucera, J. & Snider, W.D. Development of sensory neurons in the absence of NGF/TrkA signaling *in vivo*. *Neuron* **25**, 345–357 (2000).
40. Mohler, P.J. *et al.* Ankyrin-B mutation causes type 4 long-QT cardiac arrhythmia and sudden cardiac death. *Nature* **421**, 634–639 (2003).
41. Ecker, P.M. *et al.* Effect of targeted deletions of beta1- and beta2-adrenergic-receptor subtypes on heart rate variability. *Am. J. Physiol. Heart Circ. Physiol.* **290**, H192–H199 (2006).
42. Heart rate variability: standards of measurement, physiological interpretation and clinical use. Task Force of the European Society of Cardiology and the North American Society of Pacing and Electrophysiology *Circulation* **93** 1043 1065 (1996).
43. Wehrens, X.H. *et al.* Protection from cardiac arrhythmia through ryanodine receptor-stabilizing protein calstabin2. *Science* **304**, 292–296 (2004).
44. Kannankeril, P.J. *et al.* Mice with the R176Q cardiac ryanodine receptor mutation exhibit catecholamine-induced ventricular tachycardia and cardiomyopathy. *Proc. Natl. Acad. Sci. USA* **103**, 12179–12184 (2006).

Available online at www.sciencedirect.com
ScienceDirect
Journal of Molecular and Cellular Cardiology 43 (2007) 710–716
Journal of Molecular and Cellular Cardiology
www.elsevier.com/locate/yjmcc

Original article

SHP2-mediated signaling cascade through gp130 is essential for LIF-dependent I_{CaL}, $[Ca^{2+}]_i$ transient, and APD increase in cardiomyocytes

Yoko Hagiwara [a], Shunichiro Miyoshi [a,*], Keiichi Fukuda [b], Nobuhiro Nishiyama [a], Yukinori Ikegami [a], Kojiro Tanimoto [a], Mitsushige Murata [a], Eiichi Takahashi [a], Kouji Shimoda [c], Toshio Hirano [d], Hideo Mitamura [e], Satoshi Ogawa [a]

[a] *Division of Cardiology, Department of Medicine, Keio University School of Medicine, Japan*
[b] *Department of Regenerative Medicine and Advanced Cardiac Therapeutics, Keio University School of Medicine, Japan*
[c] *Laboratory Animal Center, Keio University School of Medicine, Japan*
[d] *Department of Molecular Oncology, Graduate School of Medicine, Osaka University, Japan*
[e] *Saiseikai Central Hospital, Japan*

Received 12 June 2007; received in revised form 30 August 2007; accepted 10 September 2007
Available online 19 September 2007

Abstract

Leukemia inhibitory factor (LIF), a cardiac hypertrophic cytokine, increases L-type Ca^{2+} current (I_{CaL}) via ERK-dependent and PKA-independent phosphorylation of serine 1829 in the $Cav_{1.2}$ subunit. The signaling cascade through gp130 is involved in this augmentation. However, there are two major cascades downstream of gp130, i.e. JAK/STAT3 and SHP2/ERK. In this study, we attempted to clarify which of these two cascades plays a more important role. Knock-in mouse line, in which the SHP2 signal was disrupted ($gp130^{F759/F759}$ group), and wild-type mice (WT group) were used. A whole-cell patch clamp experiment was performed, and intracellular Ca^{2+} concentration ($[Ca^{2+}]_i$ transient) was monitored. The I_{CaL} density and $[Ca^{2+}]_i$ transient were measured from the untreated cells and the cells treated with LIF or IL-6 and soluble IL-6 receptor (IL-6+sIL-6r). Action potential duration (APD) was also recorded from the ventricle of each mouse, with or without LIF. Both LIF and IL-6+sIL-6r increased I_{CaL} density significantly in WT (+27.0%, $n=16$ $p<0.05$, and +32.2%, $n=15$, $p<0.05$, respectively), but not in $gp130^{F759/F759}$ (+9.4%, $n=16$, NS, and −6.1%, $n=13$, NS, respectively). Administration of LIF and IL-6+sIL-6r increased $[Ca^{2+}]_i$ transient significantly in WT (+18.8%, $n=13$, $p<0.05$, and +32.0%, $n=21$, $p<0.05$, respectively), but not in $gp130^{F759/F759}$ (−3.8%, $n=7$, NS, and −6.4%, $n=10$, NS, respectively). LIF prolonged APD_{80} significantly in WT (10.5±4.3%, $n=12$, $p<0.05$), but not in $gp130^{F759/F759}$ (−2.1±11.2%, $n=7$, NS). SHP2-mediated signaling cascade is essential for the LIF and IL-6+sIL-6r-dependent increase in I_{CaL}, $[Ca^{2+}]_i$ transient and APD.

Keywords: IL-6; Leukemia inhibitory factor (LIF); Ion channel; L-type Ca^{2+} current; Patch clamp; Fluo-4; SHP2

1. Introduction

Leukemia inhibitory factor (LIF) is a member of the IL-6 family of cytokines that induces a wide range of responses in a variety of cells [1]. LIF is known to have various effects on cell growth, differentiation, and function [2–4]. The receptors of the IL-6 family of cytokines have common subunits, gp130 [5,6]. The binding of the IL-6 family cytokines to their receptors activates Janus kinases (JAK1, JAK2, and TYK2) [7,8], leading to the recruitment of signal transducing molecules such as protein tyrosine phosphatase 2 (SHP2) and signal transducers and activators of transcription3 (STAT3) [9–11]. It is considered that there are two major cascades downstream of gp130, i.e. JAK/STAT3 and SHP2/ERK [12,13].

In cardiomyocytes, we have reported that LIF induces cardiac hypertrophy [14]. The JAK/STAT3 pathway plays an important role in mediating this cardiac hypertrophy.

On the other hand, we have reported that LIF increases L-type Ca^{2+} current (I_{CaL}) and intracellular Ca^{2+} concentration ($[Ca^{2+}]_i$ transient) in cardiomyocytes, and this I_{CaL} augmentation is independent of PKA but dependent on mitogen-activated protein kinase (MEK) [15]. We have also reported that LIF

* Corresponding author. 35 Shinanomachi Shinjuku-ku Tokyo, Japan. Tel.: +81 3 3353 1211; fax: +81 3 3353 2502.
E-mail address: smiyoshi@cpnet.med.keio.ac.jp (S. Miyoshi).

0022-2828/$ - see front matter © 2007 Elsevier Inc. All rights reserved.
doi:10.1016/j.yjmcc.2007.09.004

phosphorylates the serine residue at the position 1829 of the $Cav_{1.2}$ subunit via the actions of extracellular signal-regulated kinase (ERK) and that this phosphorylation increases I_{CaL} in cardiomyocytes [16]. Therefore, the MEK/ERK pathway might be involved in the LIF-mediated increase of I_{CaL}. There may be, however, a possible crosstalk between the JAK/STAT3 pathway and the MEK/ERK pathway downstream of gp130, and therefore the role of the JAK/STAT3 pathway in the LIF-mediated increase of I_{CaL} remains to be elucidated.

In this study, using the knock-in mouse line, we attempted to clarify that it is not the JAK/STAT3 pathway, but rather the SHP2/ERK pathway below gp130 that plays an important role in this I_{CaL} augmentation.

2. Materials and methods

2.1. Materials

The knock-in mouse line [12], in which the SHP2 signal was disrupted by replacing the mouse gp130 gene with the human gp130 mutant cDNA ($gp130^{F759/F759}$ group), and wild-type mice (WT group) were used for this experiment. These mice were 6–10 weeks of age and weighed 21–28 g. In the $gp130^{F759/F759}$ group, only the JAK/STAT3 cascade can be activated, and both the JAK/STAT3 and SHP2/ERK cascades can be activated in the WT group.

2.2. Cell preparation for the patch clamp

After 1000 units of heparin and 50 mg of sodium pentobarbital were administered intraperitoneally, the murine heart was quickly excised and retrogradely perfused with nominally Ca^{2+}-free HEPES–Tyrode's solution, which contained 140 mmol/l NaCl, 4 mmol/l KCl, 0.5 mmol/l $MgCl_2$, 5.5 mmol/l glucose, and 5 mmol/l HEPES (pH adjusted to 7.4 with NaOH) for 3 min, and with the same solution containing 0.5 mg/ml of type II collagenase (Worthington Biochemical, NJ, USA) for 30 min at 37 °C. The ventricles were excised and were gently agitated in high-K^+ storage medium, containing 70 mmol/l glutamic acid-K, 15 mmol/l taurine, 30 mmol/l KCl, 10 mmol/l KH_2PO_4, 0.5 mmol/l EGTA, 0.5 mmol/l $MgCl_2$, 60 mmol/l glucose, and 5 mmol/l HEPES (pH adjusted to 7.4 with KOH) for 10 min to obtain isolated ventricular cells. After small cells, e.g. blood cells or non-myocyte cells, were discarded by use of 20 μm nylon mesh, isolated ventricular cells were stored in high-K^+ storage medium at room temperature for 3–4 h before the patch clamp experiment.

2.3. Whole-cell patch clamp

We performed a whole-cell patch clamp to measure I_{CaL} as described previously [15,17]. HEPES–Tyrode's solution supplemented with 0.5 mmol/l of $CaCl_2$ and 1.3 mmol/l $MnCl_2$ was used for the external solution for the patch clamp experiment. To prevent contamination with other monovalent cation currents, external Na^+ and K^+ in the bath solution were substituted by equimolar choline. The pipette solution contained 115 mmol/l CsCl, 20 mmol/l TEA–Cl, 5 mmol/l MgATP, 0.4 mmol/l TrisGTP, 10 mmol/l BAPTA, and 5 mmol/l HEPES (pH adjusted to 7.2 with CsOH). The resistance of pipettes filled with the internal solution was 1.4 to 1.8 MΩ. Seal resistances <4 GΩ and series resistances >2 MΩ were discarded from the analysis. Currents obtained in this study were normalized to each cell capacitance.

We preincubated the cells in the presence of LIF (1000 U/ml), IL-6 (20 ng/ml), and soluble IL-6 receptor (sIL-6r) (25 ng/ml) or in the absence of it (control) for 20–40 min before the measurement. The effect of PD098059, a specific MEK inhibitor, on I_{CaL} was also observed [15]. The percent inhibition curve was automatically fitted to Hill's equation: $\Delta I/\Delta I_{max} = 1 - C^n/C^n + IC_{50}^n$ by a Chi-square procedure.

See details in the Supplementary data section.

2.4. Cell preparation for the measurement of $[Ca^{2+}]_i$ transient

Instead of HEPES–Tyrode's solution, Ca^{2+}-free $NaHCO_3$-buffered Tyrode's solution, containing 126 mmol/l NaCl, 4.4 mmol/l KCl, 1.0 mmol/l $MgCl_2$, 18 mmol/l $NaHCO_3$, 11 mmol/l glucose, 4 mmol/l HEPES, and 30 mmol/l BDM (pH adjusted to 7.4 at 37 °C with oxygenation; O_2 95%/CO_2 5%), was used for the cell isolation to measure $[Ca^{2+}]_i$ transient. After the washout of blood cells for 3 min, tissue was digested in the same solution with 0.9 mg/ml of type II collagenase and 25 μmol/l of $CaCl_2$ for 15 min at 37 °C. The ventricles were minced and gently agitated in the same solution with 0.9 mg/ml of the collagenase, 20 g/l of albumin Fraction-V (A7906-50G, Sigma, MO, USA), and 200 μmol/l $CaCl_2$. Incubation with the fresh enzyme solution was repeated 3 times at 15-min intervals. The supernatant from each digestion was filtered (100-μm mesh) and centrifuged (500 rpm for 3 min). The cells were then stored in the $NaHCO_3$-buffered Tyrode's solution supplemented with the same amount of minimum essential medium (MEM; 634-04281 WAKO, Tokyo, Japan) and 1 g/l of the albumin at room temperature for 3–4 h before the $[Ca^{2+}]_i$ transient experiment.

2.5. Measurement of $[Ca^{2+}]_i$ concentration

The $[Ca^{2+}]_i$ transient was monitored by use of the fluorescent calcium indicator Fluo-4 AM (Molecular Probes, Eugene, USA), as described previously [15,18]. The $[Ca^{2+}]_i$ transient was recorded from the baseline (0 min) until 30 min after the application of LIF (1000 U/ml) or IL-6 (20 ng/ml) and sIL-6r (25 ng/ml). F/Fo ratio was defined as the following equation:

F/Fo = (Peak fluorescence intensity
−minimum fluorescence intensity)
/(Peak fluorescence intensity at baseline
−minimum fluorescence intensity at baseline)

See details in the Supplementary data section.

2.6. Action potential recordings

The action potential from the endocardium of the left ventricle was recorded by standard microelectrodes as described

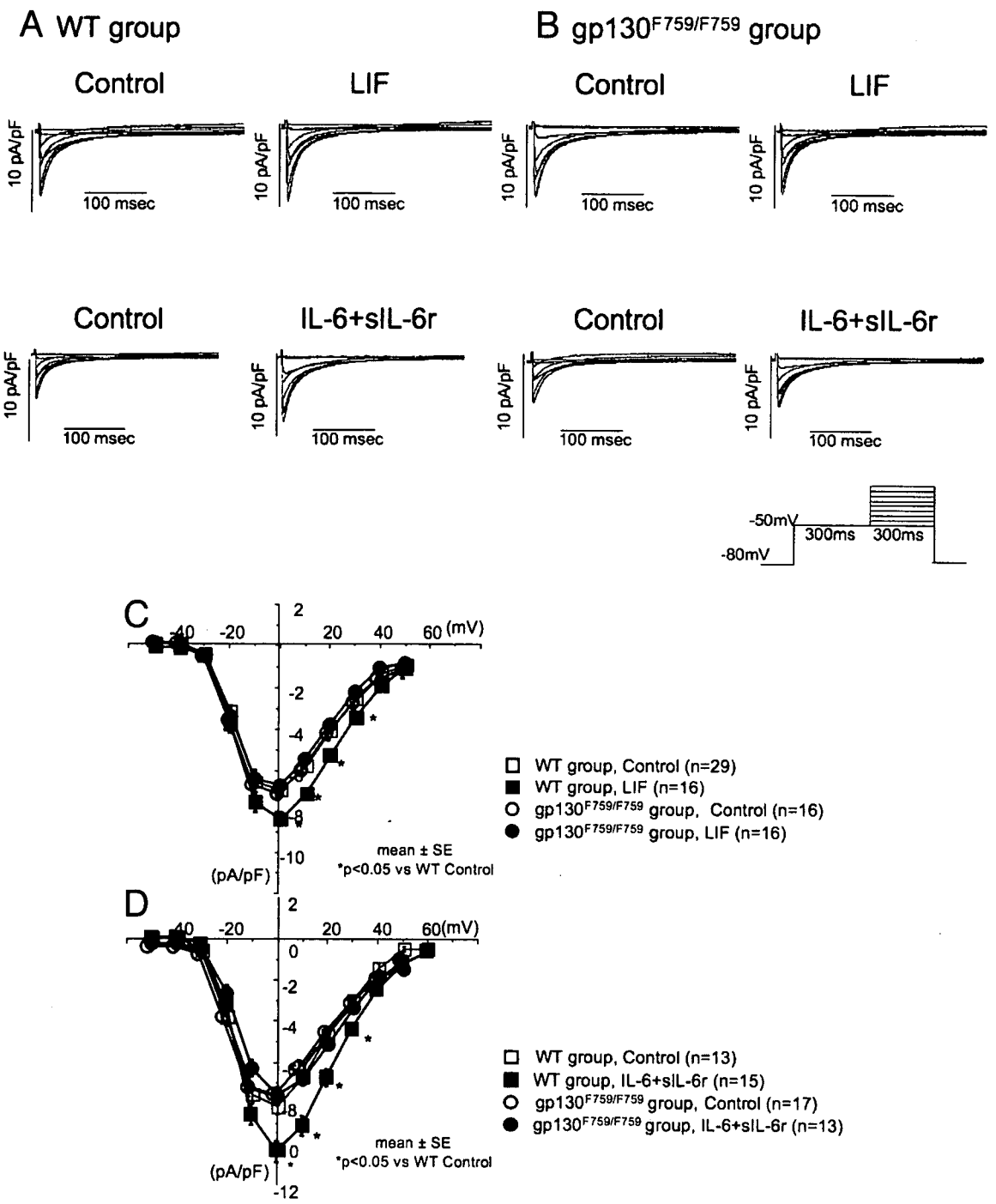

Fig. 1. (A) Representative current traces of L-type Ca^{2+} current of the WT group. (B) Representative current traces of L-type Ca^{2+} current of the $gp130^{F759/F759}$ group. Each left panel shows the control and each right panel shows the administration of LIF or IL-6+sIL-6r. The I_{CaL} elicited by the voltage-clamp protocol in the inset was normalized to the cell capacitance. (C) The current–voltage relationship of mean peak I_{CaL} density of the control and the administration of LIF. (D) The current–voltage relationship of mean peak I_{CaL} density of the control and the administration of IL-6+sIL-6r. Both LIF and IL-6+sIL-6r increased I_{CaL} density significantly in the WT group.

previously [17]. The maximum diastolic potential (MDP), the maximum positive deflection of the phase 0 upstroke (V_{max}), amplitude of the action potential (AMP), and APD at 50% and 80% repolarization (APD_{50} and APD_{80}) were measured at the 300, 250, 200, and 150 ms pacing cycle length (PCL). The measurements were made at least 30 min after the application of LIF (1000 U/ml). The data after the administration of LIF were compared with the data before the administration (baseline). See details in the Supplementary data section.

2.7. Solution and chemicals

Most reagents were purchased from Sigma (St Louis, MO, USA) and Wako (Osaka, Japan). LIF, IL-6, and sIL-6r were

purchased from Genzyme (Cambridge, MA, USA). To stimulate gp130 independently from the LIF receptor, IL-6 and sIL-6r were simultaneously administered [19].

2.8. Statistical analysis

All data are shown as the mean value±SE. The difference among mean values was determined with ANOVA for repeated measurements. The post hoc test (Bonferroni/Dunn) was used when three or more groups were compared. Student's *t*-test was used when two values were compared. Fisher exact probability test was used to test the significance of the difference in the incidence of arrhythmic activity between the groups. Statistical significance was set at $p<0.05$.

3. Results

3.1. L-type Ca^{2+} current

The cardiomyocytes isolated from the WT group and the $gp130^{F759/F759}$ group appeared similar. There was no difference in the cell capacitance between the WT group (138.5±1.9 pF) and the $gp130^{F759/F759}$ group (142.0±2.5 pF) and there was no difference in the I_{CaL} density of the control (WT group: 7.54± 0.20 pA/pF, $n=76$, $gp130^{F759/F759}$ group: 7.80±0.25 pA/pF, $n=54$, NS).

Figs. 1A and B show representative traces of the control and the administration of LIF or IL-6+sIL-6r. Figs. 1C and D show the current–voltage relationship of mean peak I_{CaL} density. Both LIF and IL-6+sIL-6r increased I_{CaL} density significantly in the WT group (7.11±0.20 pA/pF, $n=29$ to 8.34±0.33 pA/pF, $n=16$, $p<0.05$, and 8.19±0.36 pA/pF, $n=13$ to 10.40± 0.52 pA/pF, $n=15$, $p<0.05$, respectively), but not in the $gp130^{F759/F759}$ group (7.33±0.31 pA/pF, $n=16$ to 6.88± 0.25 pA/pF, $n=16$, NS, and 7.25±0.43 pA/pF, $n=17$ to 7.39± 0.34 pA/pF, $n=13$, NS, respectively).

After the administration of IL-6+sIL-6r, PD098059, a specific MEK inhibitor, blocked IL-6-dependent increase of I_{CaL} density in a dose-dependent manner. At 100 μmol/l, it completely blocked the effect of IL-6 (Fig. 2A). Fig. 2B illustrates the dose–response curve of the inhibitory effect of PD098059. The average reduction of the peak I_{CaL} was fit by the Hill's equation to yield a half-maximal inhibition concentration (IC_{50}) of 7.0 μmol/l and a Hill coefficient of 0.8. These results suggested that the IL-6-induced increase in I_{CaL} was mediated by MEK.

3.2. $[Ca^{2+}]_i$ transient

The LIF-mediated increase of I_{CaL} in cardiomyocytes suggested that LIF may also increase the $[Ca^{2+}]_i$ transient. We therefore measured the $[Ca^{2+}]_i$ transient in cardiomyocytes exposed to LIF or IL-6+sIL-6r. Figs. 3A and B shows representative tracings at the baseline and 30 min after the LIF or IL-6+sIL-6r administration. Figs. 3C and D shows the percent changes of the averaged data in the amplitude of the $[Ca^{2+}]_i$ transient (F/Fo) as a function of time.

After the administration of LIF or IL-6+sIL-6r, the $[Ca^{2+}]_i$ transient (F/Fo) was increased significantly in the WT group (+18.8%, $n=13$, $p<0.05$, and +32.0%, $n=21$, $p<0.05$, respectively), but not in the $gp130^{F759/F759}$ group (−3.8%, $n=7$, NS, and −6.4%, $n=10$, NS, respectively). $[Ca^{2+}]_i$ transients were gradually increased within 10 min after the LIF or IL-6+sIL-6r administration and reached a plateau.

After the administration of LIF or IL6/sIL6r, the incidence of so-called arrhythmic sustained increase in $[Ca^{2+}]_i$ concentration

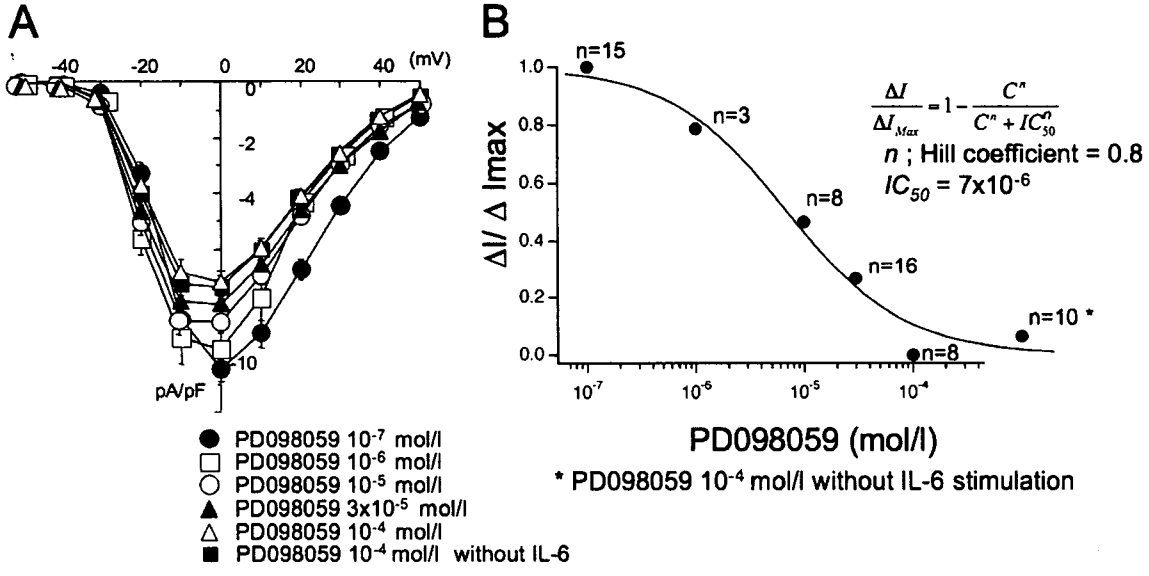

Fig. 2. Dose-dependent inhibition of PD098059, a specific MEK inhibitor of IL-6-dependent increase of I_{CaL} density. The cells were preincubated by various doses of PD098059 for 30 min and were stimulated by IL-6+sIL-6r. (A) The current–voltage relationships of mean peak I_{CaL} density are indicated. At 100 μmol/l, IL-6-dependent increase of I_{CaL} density is completely blocked. (B) The dose–response curve of the inhibitory effect of PD098059. Each plot was calculated by the following equation; $\Delta I/\Delta I_{max}$. ΔI=mean peak I_{CaL} density (each PD098059 concentration)−peak I_{CaL} density (10^{-4} mol/l PD098059 only), ΔI_{max}=mean peak I_{CaL} density (IL-6+sIL-6r only)−mean peak I_{CaL} density (10^{-4} mol/l PD098059 only). The average reduction of the peak I_{CaL} density was fit by the Hill's equation to yield a half-maximal inhibition concentration (IC_{50}) of 7.0 μmol/l and a Hill coefficient of 0.8.

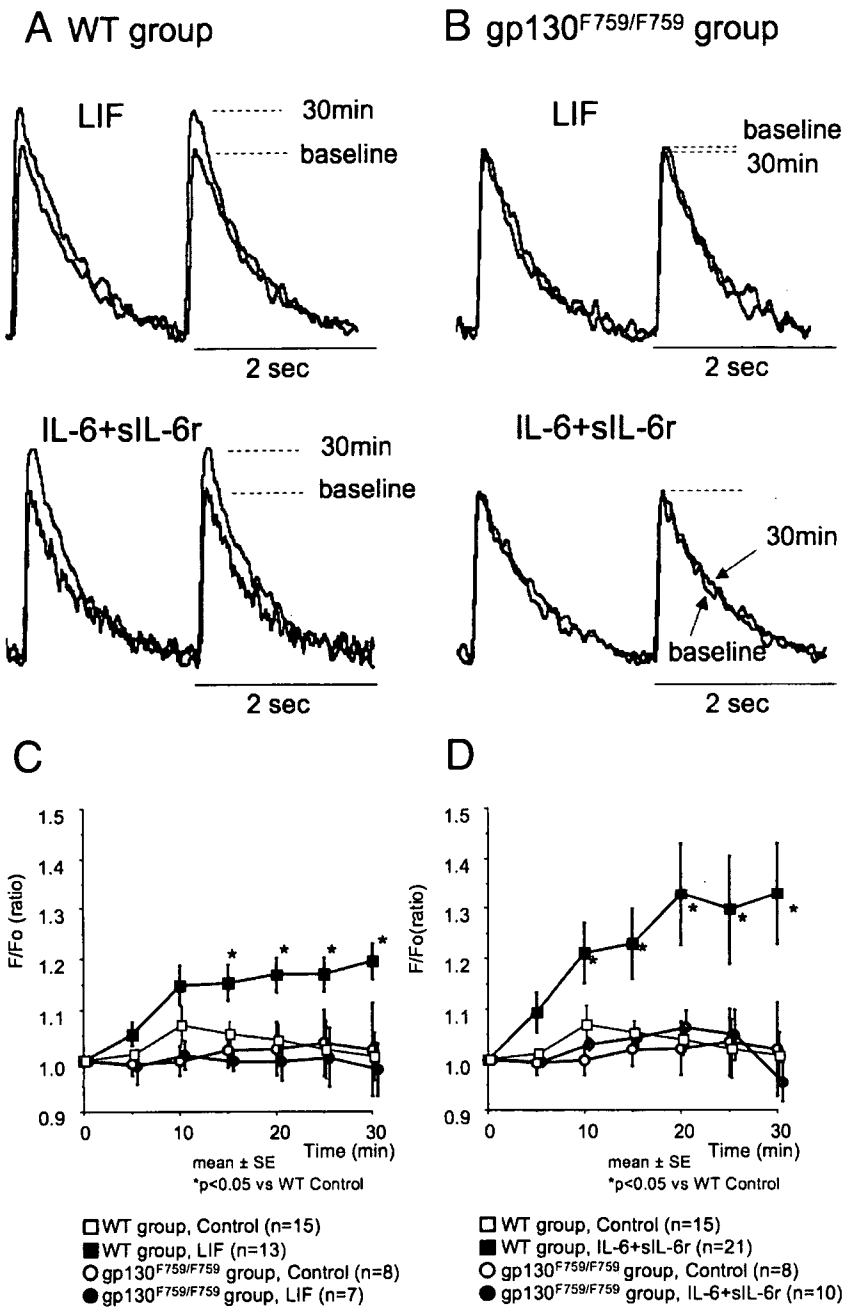

Fig. 3. (A) Representative $[Ca^{2+}]_i$ transient tracings at the baseline and 30 min after the LIF or IL-6 administration in the WT group. (B) Representative $[Ca^{2+}]_i$ transient tracings at the baseline and 30 min after the LIF or IL-6 administration to the gp130$^{F759/F759}$ group. (C) Normalized fluorescent intensity (*F*/Fo) changes of the averaged data in the amplitude of the $[Ca^{2+}]_i$ transient of the control group and LIF group, as a function of time. (D) *F*/Fo changes of the averaged data in the amplitude of the $[Ca^{2+}]_i$ transient of the control group and the administration of IL-6+sIL-6r group, as a function of the time course. Both LIF and IL-6+sIL-6r significantly increased *F*/Fo in the WT group.

was significantly higher in the WT group (8/32), than in the gp130$^{F759/F759}$ group (0/17).

3.3. Action potential

After the administration of LIF, APD_{80} was significantly prolonged in the WT group at the 200 ms PCL, compared with the gp130$^{F759/F759}$ group, but there were no differences in any other parameters measured (Table 1).

Figs. 4A and B shows representative action potential tracings at the PCL of 250 ms at the baseline and 30 min after the LIF administration. The averaged value of % change in APD_{80} (Fig. 4C) and the averaged value of APD_{80} (Fig. 4D) are shown as a function of PCL between 150 and 300 ms. LIF-induced % change in APD_{80} at the PCL was significantly longer in the WT group than in gp130$^{F759/F759}$ group.

4. Discussion

These experiments, using the knock-in mice, clarified the distinct signal transduction pathway of I_{CaL} augmentation by LIF.

Table 1
Data of action potential recordings at 200 ms pacing cycle length in the control and gp130$^{F759/F759}$ group

	WT group (n=12)		gp130$^{F759/F759}$ group (n=7)	
	Control	LIF	Control	LIF
APD_{80} (ms)	31.3±0.2	34.2±0.2*	38.2±3.9	35.2±4.6
MDP (mV)	−82.2±0.9	−83.1±1.9	−74.9±4.0	−78.3±2.3
AMP (mV)	106.5±1.4	110.0±1.9	97.2±4.8	101.3±3.2
V_{max} (V/s)	141.8±12.0	150.3±12.7	142.9±14.1	151.4±5.8

*p<0.05 vs WT control. Data are presented at the mean value±SE.
APD_{80}=action potential duration at 80% repolarization, respectively; MDP=diastolic potential; AMP=amplitude of the action potential; V_{max}= maximum positive deflection of the phase 0 upstroke.

We have reported that LIF increases I_{CaL} by the phosphorylation of the Cav1.2 subunit via the actions of ERK and that this LIF-mediated increase of I_{CaL} might be independent of PKA and involve the MEK/ERK pathway. However, the existence of crosstalk between the JAK/STAT3 and the MEK/ERK pathways could not be ruled out. In the knock-in mice, gp130$^{F759/F759}$, used in this study, Tyr-759 was replaced by a phenylalanine, and the signal below SHP2 was disrupted, while the JAK/STAT3 pathway was intact. Therefore, if there were crosstalk between the JAK/STAT3 and the MEK/ERK pathway in the gp130$^{F759/F759}$ mice, the stimulation by LIF and IL-6+ sIL-6r could activate the ERK pathway, subsequently phosphorylate the Cav1.2 subunit, and I_{CaL} could be increased. The present study showed that I_{CaL}, $[Ca^{2+}]_i$ transient, and APD were increased by LIF in the WT group, as shown above. On the other hand, in the knock-in mice gp130$^{F759/F759}$, LIF did not increase I_{CaL}, $[Ca^{2+}]_i$ transient, or APD. From these results, the SHP2/ERK-mediated signaling cascade is essential for the LIF-dependent increase in I_{CaL}, $[Ca^{2+}]_i$ transient, and APD. There was no crosstalk from the JAK/STAT3 cascade.

In the condition of heart failure, cardiac hypertrophy is induced by the mechanical load, hormonal factors, and cytokines such as angiotensin II and IL-6. LIF is known as one of these cytokines. LIF is produced from cardiomyocytes or fibroblasts by various stimuli in vivo, such as pressure overload and volume overload, and works on cardiomyocytes like autocrine or paracrine [20]. We have observed that mechanical stretch and angiotensin II stimulation rapidly increased LIF mRNA expression in cultured cardiomyocytes [21] and that LIF induces cardiac hypertrophy. On the other hand, in the present study, LIF and IL-6 increased I_{CaL}, $[Ca^{2+}]_i$ transient, and prolonged APD. Intracellular Ca^{2+} concentration is related to not only the control of cardiac contraction and relaxation, but also to the generation of cardiac arrhythmia [22]. So, in vivo, in heart failure, the cytokines such as LIF and IL-6 may increase the intracellular Ca^{2+} concentration, and it cannot be denied that this may cause cardiac arrhythmia. In fact, it was reported that the increase of IL-6 is one of the risk factors which predict sudden cardiac death in patients with coronary artery disease [23].

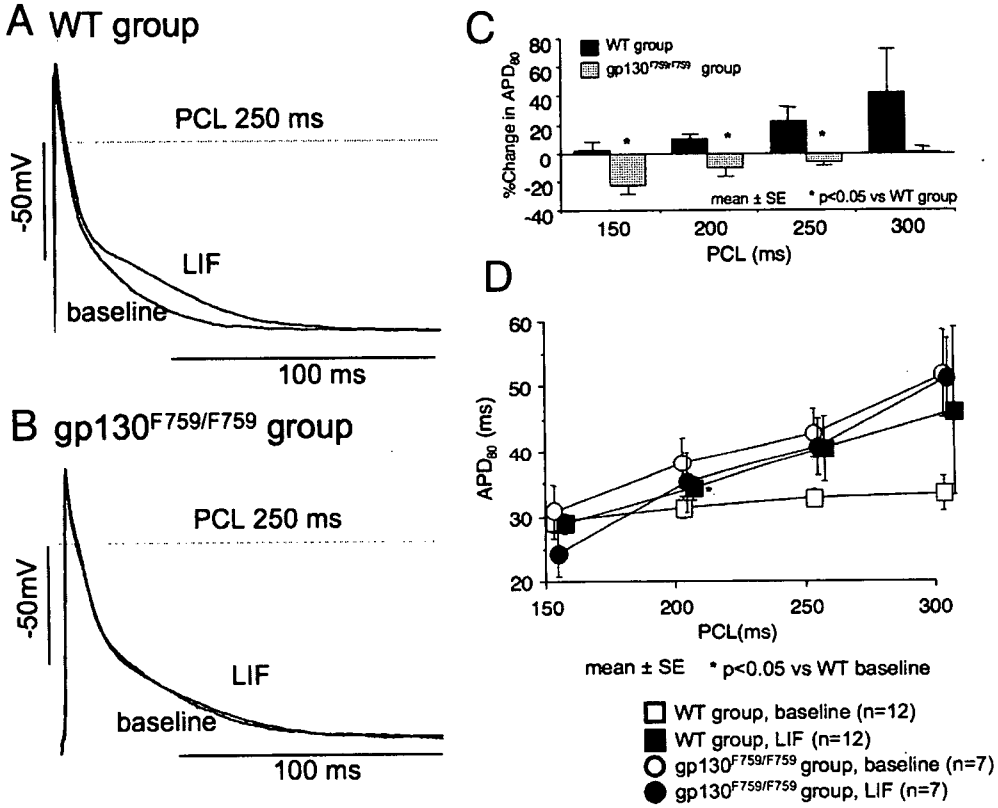

Fig. 4. (A) Representative action potential tracings at the PCL of 250 ms at the baseline and 30 min after the LIF administration in the WT group. (B) Representative action potential tracings at the PCL of 250 ms at the baseline and 30 min after the LIF administration to the gp130$^{F759/F759}$ group. (C) The averaged % change in APD_{80} as a function of PCL was shown. LIF-induced prolongation in APD_{80} was significantly (p<0.05) longer in WT group than 30$^{F759/F759}$ group. (D) The averaged data of APD_{80} are shown as a function of PCL between 150 and 300 ms.

In the present study, the arrhythmic activity in $[Ca^{2+}]_i$ transient was observed. However, we never observed early after depolarization (EAD)-like activity in the action potential experiments. These different arrhythmic responses to LIF in the different models may be due to different experimental models. It is possible that LIF and IL-6 may induce arrhythmic events under pathologic conditions [23]. We speculated that LIF and IL-6 may directly affect intracellular Ca^{2+} handling that may cause arrhythmic activity in $[Ca^{2+}]_i$ transient. Further experimentation should be required.

It has been also reported that cardiac hypertrophy is induced by the calcium-dependent phosphatase calcineurin [24]. The intracellular calcium overload, as shown in the present study, is known to be associated with signaling cascades resulting in cardiac hypertrophy. It is possible that the increase of intracellular Ca^{2+} concentration by LIF causes cardiac hypertrophy, independent from JAK/STAT activation [14].

4.1. Study limitations

We used different experimental conditions for the whole-cell patch clamp, measurement of $[Ca^{2+}]_i$ transient, and action potential recording. Such different experimental conditions may affect the result of LIF and IL-6 response. However, the effect of LIF and IL-6 was compared under the same experimental conditions as in the present study. Furthermore, the electrophysiological response for the LIF and IL-6 was consistent in every experimental set up. In order to clamp voltage accurately during I_{CaL} measurement, we used $MnCl_2$ as described in Materials and methods section. In our previous study [25] and in the present study, extracellular Mn^{2+} successfully decreased the I_{CaL} and did not affect the I_{CaL} kinetics significantly. Moreover, the effect of LIF on I_{CaL} augmentation and increase in $[Ca^{2+}]_i$ transient was observed in the absence of extracellular Mn^{2+} in our previous study [15].

Acknowledgments

This work was supported by the Suntory Fund for Advanced Cardiac Therapeutics, Keio University School of Medicine. The transgenic mouse was kindly provided from Dr. Takuya Ohtani, Osaka University School of Medicine.

Appendix A. Supplementary data

Supplementary data associated with this article can be found, in the online version, at doi:10.1016/j.yjmcc.2007.09.004.

References

[1] Metcalf D. Leukemia inhibitory factor—a puzzling polyfunctional regulator. Growth Factors 1992;7:169–73.
[2] Williams RL, Hilton DJ, Pease S, Willson TA, Stewart CL, Gearing DP, et al. Myeloid leukaemia inhibitory factor maintains the developmental potential of embryonic stem cells. Nature 1988;336:684–7.
[3] Yamamori T, Fukada K, Aebersold R, Korsching S, Fann MJ, Patterson PH. The cholinergic neuronal differentiation factor from heart cells is identical to leukemia inhibitory factor. Science 1989;246:1412–6.
[4] Metcalf D, Nicola NA, Gearing DP. Effects of injected leukemia inhibitory factor on hematopoietic and other tissues in mice. Blood 1990;76:50–6.
[5] Taga T, Hibi M, Hirata Y, Yamasaki K, Yasukawa K, Matsuda T, et al. Interleukin-6 triggers the association of its receptor with a possible signal transducer, gp130. Cell 1989;58:573–81.
[6] Hirano T, Matsuda T, Nakajima K. Signal transduction through gp130 that is shared among the receptors for the interleukin 6 related cytokine subfamily. Stem Cells 1994;12:262–77.
[7] Lutticken C, Wegenka UM, Yuan J, Buschmann J, Schindler C, Ziemiecki A, et al. Association of transcription factor APRF and protein kinase Jak1 with the interleukin-6 signal transducer gp130. Science 1994;263:89–92.
[8] Stahl N, Boulton TG, Farruggella T, Ip NY, Davis S, Witthuhn BA, et al. Association and activation of Jak-Tyk kinases by CNTF-LIF-OSM-IL-6 beta receptor components. Science 1994;263:92–5.
[9] Hirano T, Nakajima K, Hibi M. Signaling mechanisms through gp130: a model of the cytokine system. Cytokine Growth Factor Rev 1997;8:241–52.
[10] Stahl N, Farruggella TJ, Boulton TG, Zhong Z, Darnell Jr JE, Yancopoulos GD. Choice of STATs and other substrates specified by modular tyrosine-based motifs in cytokine receptors. Science 1995;267:1349–53.
[11] Yamanaka Y, Nakajima K, Fukada T, Hibi M, Hirano T. Differentiation and growth arrest signals are generated through the cytoplasmic region of gp130 that is essential for Stat3 activation. EMBO J 1996;15:1557–65.
[12] Ohtani T, Ishihara K, Atsumi T, Nishida K, Kaneko Y, Miyata T, et al. Dissection of signaling cascades through gp130 in vivo: reciprocal roles for STAT3- and SHP2-mediated signals in immune responses. Immunity 2000;12:95–105.
[13] Kunisada K, Hirota H, Fujio Y, Matsui H, Tani Y, Yamauchi-Takihara K, et al. Activation of JAK-STAT and MAP kinases by leukemia inhibitory factor through gp130 in cardiac myocytes. Circulation 1996;94:2626–32.
[14] Kodama H, Fukuda K, Pan J, Makino S, Baba A, Hori S, et al. Leukemia inhibitory factor, a potent cardiac hypertrophic cytokine, activates the JAK/STAT pathway in rat cardiomyocytes. Circ Res 1997;81:656–63.
[15] Murata M, Fukuda K, Ishida H, Miyoshi S, Koura T, Kodama H, et al. Leukemia inhibitory factor, a potent cardiac hypertrophic cytokine, enhances L-type Ca^{2+} current and $[Ca^{2+}]_i$ transient in cardiomyocytes. J Mol Cell Cardiol 1999;31:237–45.
[16] Takahashi E, Fukuda K, Miyoshi S, Murata M, Kato T, Ita M, et al. Leukemia inhibitory factor activates cardiac L-Type Ca^{2+} channels via phosphorylation of serine 1829 in the rabbit Cav1.2 subunit. Circ Res 2004;94:1242–8.
[17] Fukuda Y, Miyoshi S, Tanimoto K, Oota K, Fujikura K, Iwata M, et al. Autoimmunity against the second extracellular loop of beta(1)-adrenergic receptors induces early after depolarization and decreases in K-channel density in rabbits. J Am Coll Cardiol 2004;43:1090–100.
[18] Kato T, Sano M, Miyoshi S, Sato T, Hakuno D, Ishida H, et al. Calmodulin kinases II and IV and calcineurin are involved in leukemia inhibitory factor-induced cardiac hypertrophy in rats. Circ Res 2000;87:937–45.
[19] Chandrasekar B, Mitchell DH, Colston JT, Freeman GL. Regulation of CCAAT/enhancer binding protein, interleukin-6, interleukin-6 receptor, and gp130 expression during myocardial ischemia/reperfusion. Circulation 1999;99:427–33.
[20] Ancey C, Corbi P, Froger J, Delwail A, Wijdenes J, Gascan H, et al. Secretion of IL-6, IL-11 and LIF by human cardiomyocytes in primary culture. Cytokine 2002;18:199–205.
[21] Pan J, Fukuda K, Saito M, Matsuzaki J, Kodama H, Sano M, et al. Mechanical stretch activates the JAK/STAT pathway in rat cardiomyocytes. Circ Res 1999;84:1127–36.
[22] Zaniboni M, Yao A, Barry WH, Musso E, Spitzer KW. Complications associated with rapid caffeine application to cardiac myocytes that are not voltage clamped. J Mol Cell Cardiol 1998;30:2229–35.
[23] Fisman EZ, Benderly M, Esper RJ, Behar S, Boyko V, Adler Y, et al. Interleukin-6 and the risk of future cardiovascular events in patients with angina pectoris and/or healed myocardial infarction. Am J Cardiol 2006;98:14–8.
[24] Molkentin JD, Lu JR, Antos CL, Markham B, Richardson J, Robbins J, et al. A calcineurin-dependent transcriptional pathway for cardiac hypertrophy. Cell 1998;93:215–28.
[25] Miyoshi S, Mitamura H, Fujikura K, Fukuda Y, Tanimoto K, Hagiwara Y, et al. Mathematical model of phase 2 reentry: role of L-type Ca current. Am J Physiol 2003;284:H1285–94.

A Novel Mutation in *KCNQ1* Associated with a Potent Dominant Negative Effect as the Basis for the LQT1 Form of the Long QT Syndrome

YOSHIYASU AIZAWA, M.D., PH.D.,*† KAZUO UEDA, M.D., PH.D.,‡ FABIANA SCORNIK, PH.D.,* JONATHAN M. CORDEIRO, PH.D.,* YUESHENG WU, M.S.,* MAYURIKA DESAI, M.S.,* ALEJANDRA GUERCHICOFF, PH.D.,* YASUTOSHI NAGATA, M.D.,§ YOSHITO IESAKA, M.D.,§ AKINORI KIMURA, M.D., PH.D.,‡ MASAYASU HIRAOKA, M.D., PH.D.,‡ and CHARLES ANTZELEVITCH, PH.D.*

From the *Masonic Medical Research Laboratory, Utica, New York, USA; †Niigata University Graduate School of Medical and Dental Sciences, Niigata, Japan; ‡Tokyo Medical and Dental University, Tokyo, Japan; and §Tsuchiura Kyodo General Hospital, Ibaragi, Japan

Novel Mutation in *KCNQ1* as a Cause of LQT1. ***Introduction:*** **Long QT Syndrome (LQTS) is an inherited disorder characterized by prolonged QT intervals and life-threatening polymorphic ventricular tachyarrhythmias. LQT1 caused by *KCNQ1* mutations is the most common form of LQTS.**

Methods and Results: **Patients diagnosed with LQTS were screened for disease-associated mutations in *KCNQ1, KCNH2, KCNE1, KCNE2, KCNJ2,* and *SCN5A*. A novel mutation was identified in *KCNQ1* caused by a three-base deletion at the position 824–826, predicting a deletion of phenylalanine at codon 275 in segment 5 of *KCNQ1* (ΔF275). Wild-type (WT) and ΔF275-*KCNQ1* constructs were generated and transiently transfected together with a *KCNE1* construct in CHO-K1 cells to characterize the properties of the slowly activating delayed rectifier current (IKs) using conventional whole-cell patch–clamp techniques. Cells transfected with WT-*KCNQ1* and *KCNE1* (1:1.3 molar ratio) produced slowly activating outward current with the characteristics of IKs. Tail current density measured at −40 mV following a two-second step to +60 mV was 381.3 ± 62.6 pA/pF (n = 11). Cells transfected with ΔF275-*KCNQ1* and *KCNE1* exhibited essentially no current. (Tail current density: 0.8 ± 2.1 pA/pF, n = 11, P = 0.00001 vs WT). Cotransfection of WT- and ΔF275- *KCNQ1* (50/50), along with *KCNE1*, produced little to no current (tail current density: 10.3 ± 3.5 pA/pF, n = 11, P = 0.00001 vs WT alone), suggesting a potent dominant negative effect. Immunohistochemistry showed normal membrane trafficking of ΔF275-*KCNQ1*.**

Conclusion: **Our data suggest that a ΔF275 mutation in *KCNQ1* is associated with a very potent dominant negative effect leading to an almost complete loss of function of IKs and that this defect underlies a LQT1 form of LQTS.** *(J Cardiovasc Electrophysiol, Vol. 18, pp. 972-977, September 2007)*

ion channel, mutation, inherited syndrome, electrophysiology, Torsade de Pointes

Introduction

Long QT syndrome (LQTS) is characterized by QT prolongation in the surface ECG, syncope, and sudden cardiac death secondary to an atypical polymorphic ventricular tachycardia known as Torsade de Pointes (TdP). Mutations in 10 different genes causing inherited LQTS have been identified. Mutations in the *KCNQ1* (KvLQT1) gene can cause both the autosomal dominant Romano-Ward syndrome and the autosomal recessive Jervell and Lange-Nielsen syndrome.[1] *KCNQ1* and *KCNE1* (*minK*) form the slowly activating component of the delayed rectifier K^+ current (IKs), which contributes to cardiac repolarization. Functional expression of mutant *KCNQ1* channel proteins in heterologous expression system has revealed a loss of channel function in most cases.[1] More than 100 mutations have been identified and shown to be associated with a variety of ion channel dysfunction mechanisms.[2] The objective of this study was to evaluate the functional consequences of a novel single amino acid deletion mutant, ΔF275, in a mammalian heterologous expression system.

This study was supported by a grant from Japan Heart Foundation/Bayer Yakuhin Research Grant Abroad (YA), grant no. HL 47678 from the National Institutes of Health (CA), and the Masons of New York State and Florida.

Address for correspondence: Charles Antzelevitch, Ph.D., Masonic Medical Research Laboratory, 2150 Bleecker Street, Utica, NY 13501-1787. Fax: (315)-735-5648; E-mail: ca@mmrl.edu

Manuscript received 12 February 2007; Revised manuscript received 27 March 2007; Accepted for publication 13 April 2007.

doi: 10.1111/j.1540-8167.2007.00889.x

Methods

Clinical Case Presentation

A 14-year-old girl was referred for genetic analysis. Her ECG at annual check-up showed a prolonged QT interval of 520–560 msec. She had syncopal attack at 10 years of age, but had no family history of sudden cardiac death and normal hearing. The surface ECG at rest showed broad-based tall T wave typical LQT1[3,4] and a QTc interval of 515 ms (Fig. 1A). Holter recording and a treadmill exercise stress test did not reveal a clinically significant arrhythmia. However,

her QTc prolonged from a baseline of 475–555 msec during a treadmill exercise stress test. Infusion of epinephrine (0.3 mg/kg/min) during electrophysiological study prolonged QTc from a baseline of 470–620 msec and induced a polymorphic ventricular tachycardia (VT) (Fig. 1B). Programmed electrical stimulation in the absence of epinephrine did not induce VT or ventricular fibrillation (VF). Both parents displayed a normal ECG and genetic screening was declined.

Genetic Analysis

The protocol of this study was approved by the respective institutional review boards (IRBs) of the institutions involved in the study. After obtaining written informed consent, genomic DNA was isolated from peripheral blood lymphocytes by conventional methods.[5] The genomic DNA was amplified on GeneAmp® polymerase chain reaction (PCR) System 9700 thermal cycler by standard PCR technique using the primers as described previously.[6,7] For genetic screening, we used single-strand conformation polymorphism (SSCP), followed by DNA sequencing or PCR-sequencing method for *KCNQ1, KCNH2, SCN5A, KCNE1, KCNE2,* and *KCNJ2* genes. Abnormal conformers were sequenced with ABI377XL genetic analyzer (Applied Biosystems, Foster City, CA, USA). Electropherograms were compared with the *KCNQ1* wild-type (WT) sequence (GenBank accession number AJ006343) using the DNASIS Ver. 3.7 software (HITACHI, Japan).

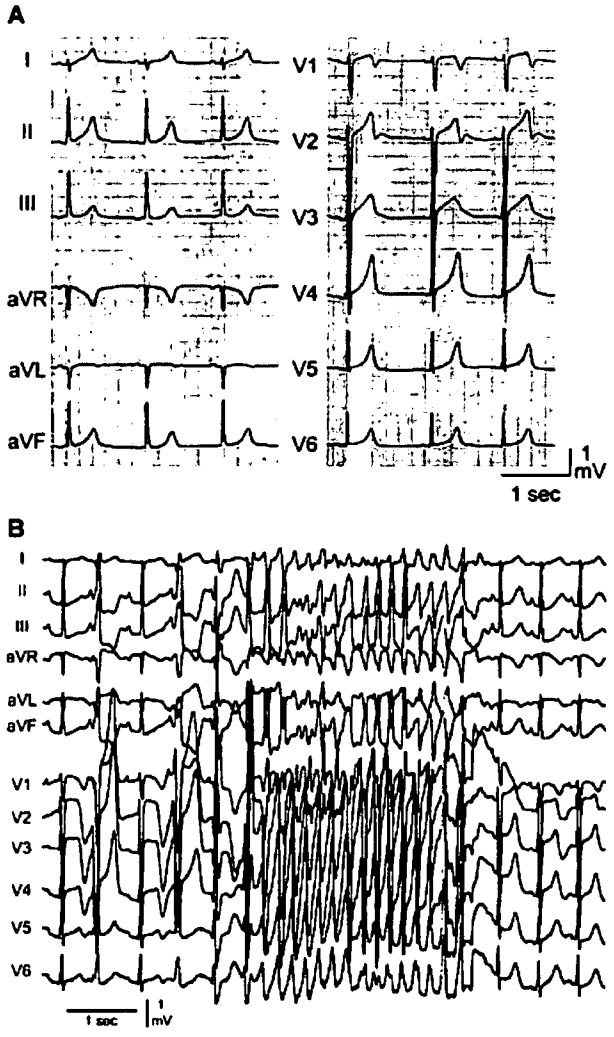

Figure 1. *Electrocardiograms of the patient. (A) Twelve-lead ECG of the patient at rest. Broad-based tall T waves are observed. QTc interval is 515 msec at rest. (B) Torsade de Pointes arrhythmias induced following administration of epinephrine (0.3 mg/kg/min). Her QTc interval prolonged to 620 msec.*

Constructs for Electrophysiological and Confocal Studies

The WT *KCNQ1* and *KCNE1* cDNAs were generated as described previously.[8] The deletion of three nucleotides, TCT, corresponding to phenylalanine at position 275 was introduced to WT-KCNQ1 cDNA by site-directed mutagenesis with primers of 5′-CGGCTTCCTGGGCCTCATCTCCTC-GTACTT-3′ and 5′-AGTACGAGGAGATGAGGCCCAGG-AAGCCG-3′. The ΔF275-KCNQ1 clone was confirmed by sequencing.

Cell Culture and Transient Transfection

CHO-K1 (Chinese hamster ovary) cells were obtained from American Type Cell Collection and cultured in Dulbecco's modified Eagle's medium (Invitrogen Corp., Carlsbad, CA, USA) supplemented with 10% fetal bovine serum and 1% penicillin-streptomycin in a humidified 5% CO_2 incubator at 37°C. Cultured cells were seeded in 35-mm dishes one day before transfection and transiently transfected with various plasmids using FuGENE6 lipid based transfection reagent (Roche Diagnostics Co., Indianapolis, IN, USA). In the electrophysiologic experiments, 0.75, 0.5, or 0.375 μg of WT-*KCNQ1* and/or 0.75, 0.375, or 0.25 μg of ΔF275-*KCNQ1*, together with 0.75 μg of WT-*KCNE1* were transfected into CHO-K1 cells. pEGFP-C1 (Clontech Laboratories Inc., Mountain View, CA, USA) was cotransfected to allow for identification of the transfected cells. Cells displaying green fluorescence 48–72 hours after transfection were studied electrophysiologically.

Electrophysiological Recordings

To investigate the effects of the ΔF275-*KCNQ1* mutation on IK_s, we performed whole-cell patch–clamp experiments on CHO-K1 cells transfected with WT- and/or ΔF275-*KCNQ1* channel. Briefly, cells were placed in a perfusion chamber (PDMI-2, Medical Systems Corp., Greenvale, NY, USA) mounted on the stage of an inverted microscope (TE2000, Nikon, USA). Cells were superfused with normal external solution containing (in mmol/L) 132 NaCl, 4.8 KCl, 2 $CaCl_2$, 1.2 $MgCl_2$, 5 Glucose, and 10 HEPES-Na (pH = 7.4 adjusted with HCl). Patch pipettes were fabricated from borosilicate glass capillaries (1.5-mm O.D., Fisher Scientific, Pittsburgh, PA). Pipettes were pulled using a gravity puller: PP-83 (Narishige, Japan) and filled with pipette solution of the following composition (mmol/L) 110 Aspartic acid, 5 ATP-K_2, 11 EGTA, 10 HEPES, and 1 $MgCl_2$ (pH = 7.35 adjusted with KOH). The pipette resistance ranged from 2–5 MΩ when filled with the internal solution. All recordings were made at room temperature.

After forming a gigaseal, the cell membrane was ruptured by applying negative pressure. Current signals were recorded using an Axopatch 200A amplifier (Axon Instruments Inc.,

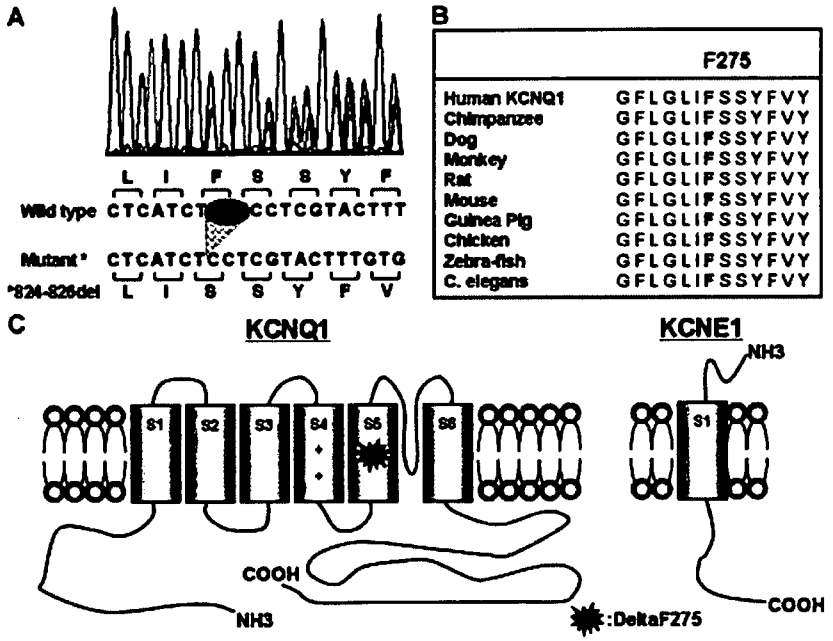

Figure 2. *Δ275F mutant at KCNQ1. (A) Chromatogram showing a heterozygous deletion at the position of 824–826. (B) Amino acid sequence alignment showing conservation of Phenylalanine 275 in multiple species. (C) Schematic topology of KCNQ1 and KCNE1 proteins forming IKs. Δ275F mutation was located at the S5 segment of KCNQ1.*

Foster City, CA, USA) and series resistance errors were reduced by 60–70% with electronic compensation. All signals were acquired at 500–5 kHz (Digidata 1322, Axon Instruments) with a personal computer running Clampex 9 software (Axon Instruments) and filtered at 5 kHz with a 4-pole Bessel low-pass filter. Membrane currents were analyzed with Clampfit 9 software (Axon Instruments).

Immunohistochemistry

Immunohistochemistry was performed to assess protein localization of WT- and ΔF275- *KCNQ1* channels. Briefly, CHO-K1 cells transfected with WT- and/or ΔF275-*KCNQ1* were fixed with an ethanol–acetone mixture and permeabilized with 0.2% Triton X-100. Cells were incubated overnight at 4°C with 1:100/200 dilutions of primary goat polyclonal antibodies against the *KCNQ1* channel protein (Santa Cruz Biotechnology Inc., Santa Cruz, CA, USA) 48 hours after transfection. Cells were incubated with a 1:1,000 dilution of antigoat alexa-488 conjugated secondary antibody (Molecular Probes, Eugene, OR, USA) for 2 hours at room temperature. Cells were mounted using Pro-Long antifade mounting media (Molecular Probes).

Immunofluorescence-stained CHO-K1 cells were visualized by confocal microscopy (Olympus Fluoview FV300). Cells were excited at 488 nm, using an argon laser, and emission was collected via 525 nm band pass filter and photomultiplier tube (40X oil immersion lens).

Statistics

Results are expressed as mean ± S.E.M. Difference between groups were tested by one-way ANOVA followed by Scheffe's modified *F*-test for multiple comparisons. Values of $P < 0.05$ were considered statistically significant.

Results

We initially evaluated DNA from the patient for mutations in the *KCNQ1* gene, using SSCP analysis of PCR product. An abnormal pattern of bands was detected in exon 6. Further examination by direct sequencing of the abnormal fragment showed a deletion of TCT at position 824–826 in *KCNQ1* (Fig. 2A). This abnormal sequence causes a single amino acid deletion of phenylalanine at position 275 in the S5 segment of *KCNQ1* channel. The phenylalanine at position 275 is highly conserved among different species. (Fig. 2B) Predicted topology of WT- and mutant-*KCNQ1* channel is shown in Figure 2C. This mutation was not detected in more than 200 unrelated ethnically matched healthy individuals. No mutations were identified in any of the other long QT-related genes screened (*KCNH2, KCNE1, KCNE2, SCN5A*).

Conventional whole-cell patch–clamp experiments were conducted on cells transfected with WT- and/or mutant-*KCNQ1*. Representative current traces of each transfection protocols are shown in Figure 3A–E. Cells transfected with 0.75 μg of WT-*KCNQ1* together with 0.75 μg of *KCNE1* exhibited slowly activating outward current compatible with IKs recorded from native cardiac myocytes (Fig. 3A), whereas cells transfected with same amount of ΔF275-*KCNQ1*+*KCNE1* produced little to no current (Fig. 3E). Cells transfected with 0.375 μg of WT-*KCNQ1* (+*KCNE1*) expressed slightly less IKs, compared with those transfected with 0.75 μg of WT-KCNQ1, although the differences were not statistically significant (Fig. 3B). Coexpression of 0.375 μg of WT-*KCNQ1* with the same amount of ΔF275-*KCNQ1* (+ *KCNE1*) showed little to no current (Fig. 3D). Increasing the ratio of WT to ΔF275 from 1:1 to 2:1 resulted in a slight recovery of IKs current (Fig. 3C). These observations indicate a potent dominant negative effect of ΔF275-*KCNQ1*.

Summary data of current-voltage relationships for peak current recorded and tail currents recorded upon repolarization to −40 mV for the various transfection protocols are shown graphically in Figure 4A,B. Current–voltage relations were not significantly different between 0.75 and 0.375 μg of WT. I-V relation for Δ275F-*KCNQ1* channels was nearly flat and significantly different from WT ($P = 0.00001$). Cotransfection of WT- and ΔF275- *KCNQ1* (1:1) along with *KCNE1*

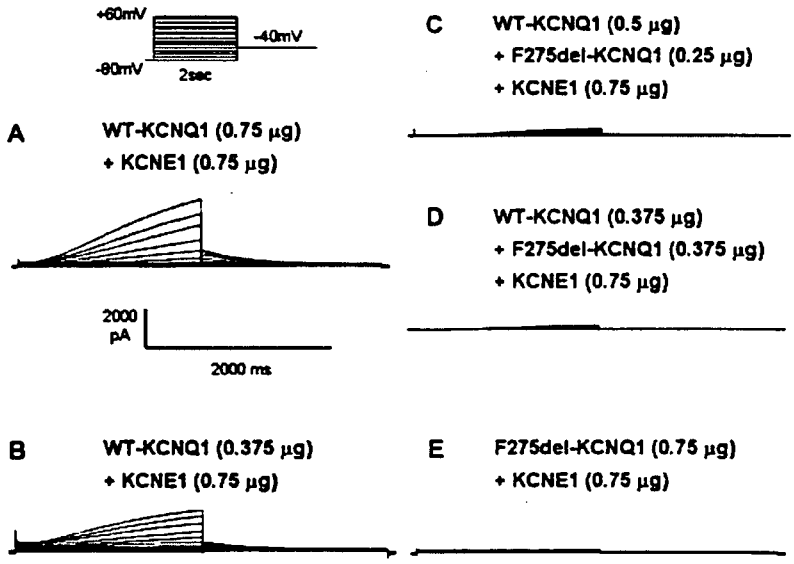

Figure 3. *Representative current traces of WT- and/or Δ275F-KCNQ1 expressed in CHO-K1 cells. Cells of each panel were transfected as follows: (A) 0.75 μg of WT-KCNQ1 and 0.75 μg of KCNE1. (B) 0.375 μg of WT-KCNQ1 and 0.75 μg of KCNE1. (C) 0.5 μg of WT-KCNQ1, 0.25 μg of Δ275F-KCNQ1, and 0.75 μg of KCNE1. (D) 0.375 μg of WT-KCNQ1, 0.375 μg of Δ275F-KCNQ1, and 0.75 μg of KCNE1. (E) 0.75 μg of Δ275F-KCNQ1 and 0.75 μg of KCNE1. Pulse protocol is shown in the inset at the top.*

also produced little to no current (P = 0.00001 vs WT). Increasing WT to ΔF275-*KCNQ1* ratio from 1:1 to 2:1 significantly increased developing current (P = 0.00251). Summary data for current intensity recorded during depolarizations to +60 mV and tail currents recorded upon repolarization to –40 mV shown in Figure 4C,D. These results once again indicate that the ΔF275-*KCNQ1* mutant exerts a very potent dominant negative effect on channel function or expression.

To determine whether the changes observed on IKs are due to impaired trafficking of the protein to the plasma membrane, we determined the localization of WT and mutant *KCNQ1* channel proteins using immunohistochemical techniques.

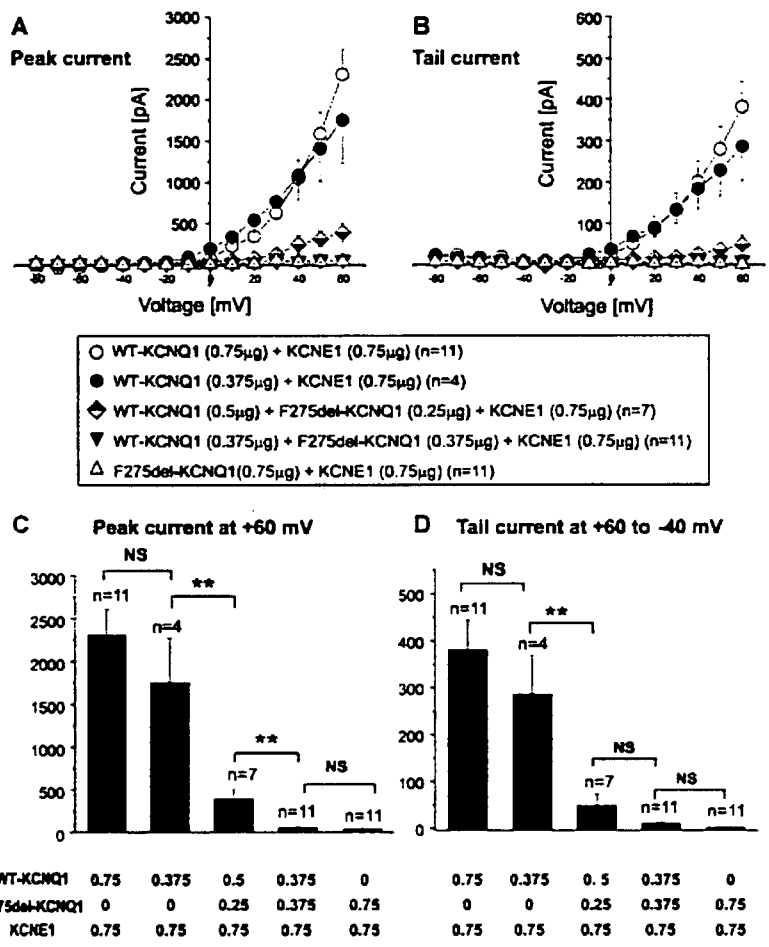

Figure 4. *Current-Voltage relationships of expressed currents. (A) Current-Voltage relationship measured at the peak current during the test depolarization pulse. (B) Current–Voltage relationship measured of the tail current upon repolarization to −40 mV following test depolarization. (C) Bar graphs showing current densities of developing (peak) recorded current at +60 mV. (D) Bar graphs showing current densities of tail current recorded upon repolarization to −40 mV from +60 mV test depolarization.*

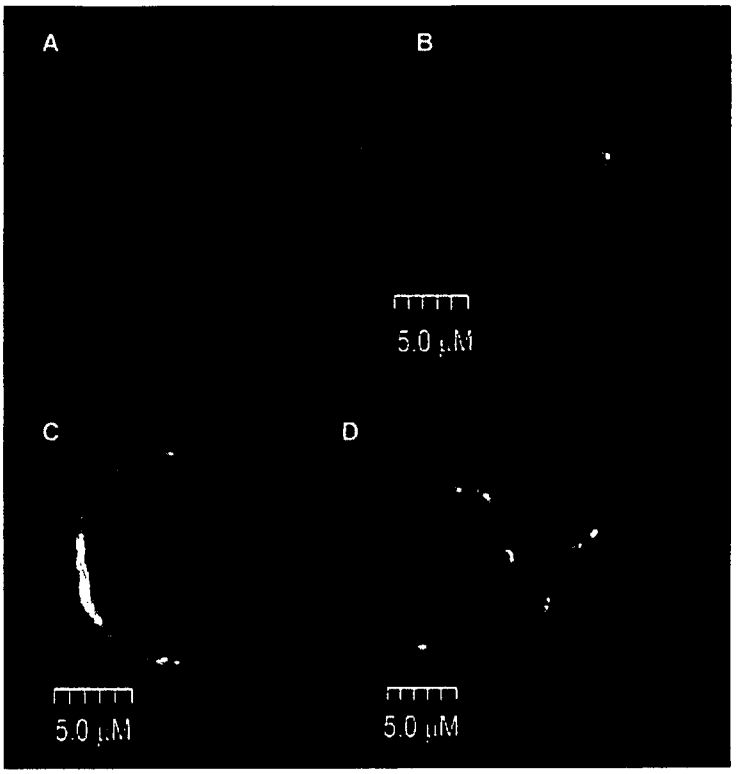

Figure 5. *Protein localization of WT- and/or mutant-KCNQ1 in CHO-K1 cells visualized by immunohistochemistry. Figure shows 0.15 μm optical sections from the center of CHO-K1 cells transfected with WT-KCNQ1 (B), ΔF275-KCNQ1 (C) or ΔF275-KCNQ1 + WT (D). A brighter fluorescence intensity near the plasma membrane reveals positive immunostaining of the KCNQ1 channel. Panel A shows the lack of any fluorescence signal from nontransfected cells.*

CHO-K1 transfected with WT-*KCNQ1* and/or ΔF275-*KCNQ1* cells were incubated with a goat polyclonal antibody against the KCNQ1 channel protein. Localization of the immunolabeled protein was assessed by confocal imaging, following incubation of the cells with an Alexa-488 conjugated secondary antigoat antibody. Positive staining was observed only in transfected CHO-K1 cells, but not in nontransfected controls (Figure 5A). Cells transfected with WT (Fig. 5B), ΔF275-*KCNQ1* (Fig. 5C), or WT + ΔF275-*KCNQ1* (Fig. 5D) all displayed peripheral staining. Similar results were obtained in 15 cells transfected with WT (four transfections), 14 cells transfected with ΔF275-*KCNQ1* (four transfections), and five cells transfected with WT + ΔF275-*KCNQ1* (two transfections).

These findings suggest that the loss of function observed with the ΔF275 mutant is not due to a defect in trafficking of mature KCNQ1 channels from the ER/Golgi complex to the cell membrane.

Discussion

LQT1 is caused by gene mutations in *KCNQ1* and is the most common form of congenital LQTS, responsible for approximately 43% of LQTS-linked mutations. *KCNQ1* encodes the pore-forming alpha-subunit of the IK_s potassium channel. *KCNE1* encodes the beta-subunit. More than 100 mutations in *KCNQ1* have been reported to cause a loss of function and thus, to predispose to the development of LQTS. Reduced levels of IK_s lead to prolongation of action potential duration (APD) and thus, to prolongation of the QT interval and the development of TdP. The present study identifies a novel *KCNQ1* mutation (F275del or ΔF275) caused by a three-nucleotide deletion, resulting in deletion of a phenylalanine in the S5 segment of *KCNQ1*. Functional analysis of the mutated channel protein revealed a major loss of function consistent with the LQT1 phenotype of the patient.

The ΔF275-*KCNQ1* channel failed to produce any current when coexpressed with *KCNE1*, indicating that the mutant was unable to form functional homomultimeric channels or could not be expressed on the surface membrane due to a trafficking defect. Subcellular localization of the channel proteins revealed normal trafficking of the mutant protein, thus pointing to a functional dysfunction of the channel as the cause for the loss of current. Coexpression of WT- and ΔF275-*KCNQ1* channel produced little to no IK_s, suggesting that the ΔF275-*KCNQ1* suppresses the function of the WT channel in a potent dominant negative manner. Thus, the heteromultimeric channel containing mutant subunits is largely nonfunctional. The strong dominant negative suppression is consistent with the clinical phenotype observed in our patient with QTc intervals at rest as long as 560 msec, which prolonged by 150 msec in response to epinephrine infusion, leading to induction of TdP. The ΔQTc induced by epinephrine is longer than that observed in LQT1 patients with the Romano–Ward syndrome.[9,10] These characteristics approach those described for patients with Jervell and Lange–Nielsen syndrome, the homozygous recessive form of LQT1.[11] Although several dominant-negative *KCNQ1* mutants have been reported,[8,12–15] the ΔF275-*KCNQ1* mutation herein described appears to result in the most prominent dominant-negative suppression of IK_s.

A number of mutations in *KCNQ1* have been shown to cause trafficking defects, leading to haploinsufficiency (T587M and ΔS276) or a dominant negative effect

(A178fs/105). These variations are often missense mutations in the N-terminus, S5, pore region, or C-terminus.[8,16,17] Recent studies indicate that specific regions of KCNQ1 (N-terminal juxtamembranous domain or C-terminus amino acids 610–620) are critical for channel surface expression.[18,19] However, mutations outside these domains can lead to trafficking problems of varying degrees.[20] In the case of the *KCNH2* channel, the C-terminus region, including the cyclic nucleotide binding domain, is thought to be essential for channel trafficking because it contains a crucial sequence linked to endoplasmic reticulum retention and the interaction site with GM130 required for channel protein trafficking.[21] In the present study, the mutation affected the mid-portion of the S5 segment and no trafficking defect was detected.

The IK_s channel is comprised of four *KCNQ1* subunits. In the case of a heterozygous mutation in *KCNQ1*, as in the present case, mutant and WT subunits may combine to form a heteromultimeric channel. When the mutant *KCNQ1* subunits interfere with the function of the WT subunits, IK_s will be reduced by more than 50%. This greater than expected loss of function is referred to as a dominant negative effect. Mutations in the pore region, as in the case of ΔF275-*KCNQ1*, are more likely to produce a dominant negative effect.[12,22] In contrast to ΔF275-KCNQ1, the molecular phenotype of ΔS276-*KCNQ1* has a very weak dominant negative effect, leading to a recessive form of LQTS.[17]

In summary, we have identified a novel single amino acid deletion in domain five of *KCNQ1* in a patient with LQTS. Functional analysis revealed normal trafficking nonfunctioning channel with very strong dominant-negative suppression of IK_s, consistent with a pronounced LQTS phenotype and sensitivity to epinephrine.

Acknowledgments: We thank Tabitha Carrier for expert technical support and Drs. Yoshifusa Aizawa, Serge Sicouri, and Guido Pollevick for helpful discussions.

References

1. Kass RS, Moss AJ: Long QT syndrome: Novel insights into the mechanisms of cardiac arrhythmias. J Clin Invest 2003;112:810-815.
2. Roden DM: Long- QT syndrome: Reduced repolarization reserve and the genetic link. J Intern Med 2006;259:59-69.
3. Moss AJ, Zareba W, Benhorin J, Locati EH, Hall WJ, Robinson JL, Schwartz PJ, Towbin JA, Vincent GM, Lehmann MH, Keating MT, MacCluer JW, Timothy KW: ECG T-wave patterns in genetically distinct forms of the hereditary long QT syndrome. Circulation 1995;92:2929-2934.
4. Zhang L, Timothy KW, Vincent GM, Lehmann MH, Fox J, Giuli LC, Shen J, Splawski I, Priori SG, Compton SJ, Yanowitz F, Benhorin J, Moss AJ, Schwartz PJ, Robinson JL, Wang Q, Zareba W, Keating MT, Towbin JA, Napolitano C, Medina A: Spectrum of ST-T-wave patterns and repolarization parameters in congenital long-QT syndrome: ECG findings identify genotypes. Circulation 2000;102:2849-2855.
5. Schulze-Bahr E, Haverkamp W, Wiebusch H, Schulte H, Hordt M, Borggrefe M, Breithardt G, Assmann G, Funke H: Molecular analysis at the Harvey Ras-1 gene in patients with long QT syndrome. J Mol Med 1995;73:565-569.
6. Splawski I, Shen J, Timothy KW, Vincent GM, Lehmann MH, Keating MT: Genomic structure of three long QT syndrome genes: KVLQT1, HERG, and KCNE1. Genomics 1998;51:86-97.
7. Neyroud N, Richard P, Vignier N, Donger C, Denjoy I, Demay L, Shkolnikova M, Pesce R, Chevalier P, Hainque B, Coumel P, Schwartz K, Guicheney P: Genomic organization of the KCNQ1 K+ channel gene and identification of C-terminal mutations in the long-QT syndrome. Circ Res 1999;84:290-297.
8. Aizawa Y, Ueda K, Wu LM, Inagaki N, Hayashi T, Takahashi M, Ohta M, Kawano S, Hirano Y, Yasunami M, Aizawa Y, Kimura A, Hiraoka M: Truncated KCNQ1 mutant, A178fs/105, forms hetero-multimer channel with wild-type causing a dominant- negative suppression due to trafficking defect. FEBS Lett 2004;574:145-150.
9. Shimizu W, Noda T, Takaki H, Nagaya N, Satomi K, Kurita T, Suyama K, Aihara N, Sunagawa K, Echigo S, Miyamoto Y, Yoshimasa Y, Nakamura K, Ohe T, Towbin J, Priori SG, Kamakura S: Diagnostic value of epinephrine test for genotyping LQT1, LQT2 an LQT3 forms of congenital long QT syndrome. Heart Rhythm 2004;1:276-283.
10. Vyas H, Hejlik J, Ackerman MJ: Epinephrine QT stress testing in the evaluation of congenital long-QT syndrome: Diagnostic accuracy of the paradoxical QT response. Circulation 2006;113:1385-1392.
11. Goldenberg I, Moss AJ, Zareba W, McNitt S, Robinson JL, Qi M, Towbin JA, Ackerman MJ, Murphy L: Clinical course and risk stratification of patients affected with the Jervell and Lange-Nielsen syndrome. J Cardiovasc Electrophysiol 2006;17:1161-1168.
12. Shalaby FY, Levesque PC, Yang WP, Little WA, Conder ML, Jenkins-West T, Blanar MA: Dominant-negative KvLQT1 mutations underlie the LQT1 form of long-QT syndrome. Circulation 1997;96:1733-1736.
13. Wang Z, Tristani-Firouzi M, Xu Q, Lin M, Keating MT, Sanguinetti MC: Functional effects of mutations in KvLQT1 that cause long QT syndrome. J Cardiovasc Electrophysiol 1999;10:817-826.
14. Thomas D, Wimmer AB, Karle CA, Licka M, Alter M, Khalil M, Ulmer HE, Kathofer S, Kiehn J, Katus HA, Schoels W, Koenen M, Zehelein J: Dominant-negative I(Ks) suppression by KCNQ1-DeltaF339 potassium channels linked to Romano-Ward syndrome. Cardiovasc Res 2005;37:487-497.
15. Boulet IR, Raes AL, Ottschytsch N, Snyders DJ: Functional effects of a KCNQ1 mutation associated with the long QT syndrome. Cardiovasc Res 2006;70:466-474.
16. Yamashita F, Horie M, Kubota T, Yoshida H, Yumoto Y, Kobori A, Ninomiya T, Kono Y, Haruna T, Tsuji K, Washizuka T, Takano M, Otani H, Sasayama S, Aizawa Y: Characterization and subcellular localization of KCNQ1 with a heterozygous mutation in the C terminus. J Mol Cell Cardiol 2001;33:197-207.
17. Gouas L, Bellocq C, Berthet M, Potet F, Demolombe S, Forhan A, Lescasse R, Simon F, Balkau B, Denjoy I, Hainque B, Baro I, Guicheney P: New KCNQ1 mutations leading to haploinsufficiency in a general population: Defective trafficking of a KvLQT1 mutant. Cardiovasc Res 2004;63:60-68.
18. Kanki H, Kupershmidt S, Yang T, Wells S, Roden DM: A structural requirement for processing the cardiac K+ channel KCNQ1. J Biol Chem 2004;279:33976-33983.
19. Dahimene S, Alcolea S, Naud P, Jourdon P, Escande D, Brasseur R, Thomas A, Baro I, Merot J: The N-terminal juxtamembranous domain of KCNQ1 is critical for channel surface expression: Implications in the Romano-Ward LQT1 syndrome. Circ Res 2006;99:1076-1083.
20. Wilson AJ, Quinn KV, Graves FM, Bitner-Glindzicz M, Tinker A: Abnormal KCNQ1 trafficking influences disease pathogenesis in hereditary long QT syndromes (LQT1). Cardiovasc Res 2005;67:476-486.
21. Roti EC, Myers CD, Ayers RA, Boatman DE, Delfosse SA, Chan EK, Ackerman MJ, January CT, Robertson GA: Interaction with GM130 during HERG ion channel trafficking. Disruption by type 2 congenital long QT syndrome mutations. Human Ether-a-go-go-Related Gene. J Biol Chem 2002;277:47779-47785.
22. Wollnik B, Schroeder BC, Kubisch C, Esperer HD, Wieacker P, Jentsch TJ: Pathophysiological mechanisms of dominant and recessive KVLQT1 K+ channel mutations found in inherited cardiac arrhythmias. Hum Mol Genet 1997;6:1943-1949.